Journal of Molecular Neuroscience (2026) 76:67
https://doi.org/10.1007/s12031-026-02528-7

RESEARCH

Construction of a Computationally Inferred Single-Cell miRNA Activity Atlas and Analysis of Regulatory Networks in Spinal Cord Injury

Changli Xu[1] · Bingxuan Wang[2] · Zhengqiang Li[1] · Suchi Qiao[2] · Jianli Bu[1]

Received: 12 January 2026 / Accepted: 19 April 2026

Abstract

Background. Spinal cord injury (SCI) is a debilitating neurological disorder characterized by complex pathological processes involving dynamic responses of multiple cell types and intricate regulatory networks. Although single-cell RNA sequencing (scRNA-seq) has been employed to dissect cellular heterogeneity in SCI, the activity and regulatory functions of microRNAs (miRNAs) at single-cell resolution remain largely unexplored. Methods. This study utilized the GSE189070 dataset, integrating single-cell transcriptomic data from mouse spinal cord tissues at eight time points: uninjured control and 0.5, 1, 3, 7, 14, 60, and 90 days post-injury. Following quality control, batch correction, and cell-type annotation, miRNA activities across 12 major cell types were computationally inferred using a motif enrichment-based approach. Temporal clustering of miRNA activity was performed with Mfuzz, and subsequent analyses included target gene prediction, functional enrichment, and network construction. Inferred miRNA activity patterns were validated using an independent bulk miRNA sequencing dataset (GSE90452). Key findings were experimentally verified in BV-2 microglial cells and C8-D1A astrocytes using miRNA inhibitors and mimics. Results. We successfully constructed a single-cell transcriptomic atlas and a dynamic computationally inferred miRNA activity landscape during SCI progression. Independent dataset validation confirmed that inferred miRNA activity changes (e.g., mmu-miR-488-3p, mmu-miR-132-3p) were consistent with actual miRNA expression alterations. Our analysis revealed that microglia and macrophages exhibited dynamic miRNA activity patterns closely associated with inflammatory pathways, including TNFA_SIGNALING_VIA_NFKB and TOLL-LIKE RECEPTOR signaling. Cross-cell-type comparison identified 38 common differentially active miRNAs shared between microglia and macrophages, with network analysis revealing coordinated regulation of key inflammatory genes (e.g., Lif, Csf1, Il18rap). In astrocytes, specific miRNAs (e.g., miR-7a-5p, miR-124-3p) were found to regulate apoptotic pathways by targeting Casp3 and Bcl2 family genes. Experimental validation confirmed that miR-130a-3p promotes microglial inflammation, while miR-7a-5p inhibits astrocyte apoptosis under oxidative stress. Conclusion. This study presents a computationally inferred, experimentally validated single-cell-resolution map of miRNA activity dynamics during SCI, revealing potential regulatory networks in key cell types. The concordance between computational inference and independent experimental data supports the biological plausibility of our findings and provides a foundation for further therapeutic exploration.

Keywords Single-cell RNA sequencing · miRNA activity · Spinal cord injury · Microglia · Inflammatory regulation · Apoptotic pathway

Introduction

Spinal cord injury (SCI) represents a severe neurological condition that results in profound sensory, motor, and autonomic dysfunction(Anjum et al. 2020). The pathological progression of SCI involves not only primary mechanical damage to neurons and axons but also a cascade of secondary responses, including neuroinflammation, glial activation, vascular disruption, and apoptotic cell death(Sunshine et al.

✉ Jianli Bu
doctorbujianli@163.com

[1] Department of Orthopedics, Bethune International Peace Hospital, Zhongshan West Road, Shijiazhuang, 050000, P. R. China

[2] Department of Orthopedics, The Third Affiliated Hospital of Naval Medical University, Shanghai, P. R. China

Published online: 25 April 2026

2023, Wang et al. 2025). These dynamic cellular and molecular events collectively shape the post-injury microenvironment and critically influence neurological recovery(Li et al. 2025, Qin et al. 2023). Therefore, a systematic understanding of cell type-specific responses and regulatory networks following SCI is essential for uncovering its underlying mechanisms and developing effective therapeutic strategies.

In recent years, single-cell RNA sequencing (scRNA-seq) has emerged as a powerful tool for dissecting cellular heterogeneity, state transitions, and gene regulatory networks at unprecedented resolution(Ma et al. 2023). Studies utilizing scRNA-seq have revealed distinct cellular subpopulations and transcriptional dynamics in various neurological disorders(Sirkis et al. 2023), including stroke and neurodegenerative diseases (Wang et al. 2024). In the context of SCI, scRNA-seq has begun to elucidate cell type-specific transcriptional changes and intercellular crosstalk during injury progression (Zhang et al. 2023). However, a comprehensive, time-resolved atlas of cellular responses across the acute to chronic phases of SCI remains limited, particularly regarding the role of post-transcriptional regulators such as microRNAs (miRNAs).

MiRNAs are small non-coding RNAs of approximately 22 nucleotides that regulate gene expression post-transcriptionally by binding to the 3′ untranslated regions (3′UTRs) of target mRNAs, leading to mRNA degradation or translational repression (Lu and Rothenberg 2018). In SCI, miRNAs have been implicated in key pathological processes, including neuroinflammation, glial scar formation, axonal regeneration, and cell survival (Xiong et al. 2022, Gao et al. 2023). Despite their recognized importance, most studies on miRNA function in SCI have relied on bulk tissue analyses, which mask cell type-specific regulatory activities(Silvestro and Mazzon 2022). Recent methodological advances now allow for the inference of miRNA activity from scRNA-seq data based on motif enrichment analysis (miReact), enabling the exploration of miRNA function at single-cell resolution (Zhang et al. 2023). This approach provides a promising avenue to uncover cell type-specific miRNA regulatory networks in complex tissues such as the injured spinal cord.

In this study, we leveraged a publicly available scRNA-seq dataset (GSE189070) spanning eight time points from acute to chronic SCI to construct a dynamic, single-cell-resolved map of computationally inferred miRNA regulatory activity. By integrating computational approaches—including temporal clustering, target prediction, pathway enrichment, and network analysis—we aimed to elucidate the regulatory roles of miRNAs in key cell types such as microglia, macrophages, and astrocytes. Our findings not only map the spatiotemporal dynamics of miRNA activity post-SCI but also identify functional modules through which miRNAs coordinate inflammatory and apoptotic responses, providing novel mechanistic insights and potential therapeutic targets for SCI.

Materials and Methods

Data Source and Inclusion Criteria

The single-cell RNA sequencing (scRNA-seq) data used in this study were obtained from the NCBI Gene Expression Omnibus (GEO) database under accession number GSE189070. The dataset consists of 8 mouse spinal cord samples: 1 sham control (uninjured) and 7 spinal cord injury (SCI) samples at 0.5, 1, 3, 7, 14, 60, and 90 days post-injury. All samples were derived from C57BL/6 mice, and library preparation and sequencing were performed using the 10x Genomics Chromium™ Single Cell 3′ RNA-seq platform. Sample inclusion criteria were as follows: sequencing quality ≥ Q30, cell viability > 80%, and data integrity verified prior to analysis.

Preprocessing and Quality Control of Single-Cell Data

Raw sequencing data were aligned to the mouse reference genome (mm10) and gene expression matrices were generated using Cell Ranger (v6.1.2). Quality control and filtering were performed using Seurat (v4.3.0) with the following criteria: cells with 200–5,000 detected genes were retained; cells with mitochondrial gene content > 20% were excluded; cells with high hemoglobin gene expression (indicative of red blood cell contamination) were removed; and doublets were predicted and excluded using DoubletFinder (v2.0.3) with an expected doublet rate of 5%. A total of 75,183 high-quality single cells were retained for downstream analyses.

Batch Correction, Dimensionality Reduction, and Cell Clustering

To mitigate batch effects between samples, the gene expression matrices were integrated and corrected using Harmony (v1.0). Data were normalized and variance-stabilized using

the SCTransform method]. Principal component analysis (PCA) was performed, and the top 30 principal components were selected for downstream analysis. Uniform Manifold Approximation and Projection (UMAP) was applied for nonlinear dimensionality reduction. Unsupervised clustering was conducted using the Louvain algorithm at a resolution of 1.0, yielding 30 transcriptionally distinct clusters.

Cell Type Annotation

Cell types were annotated based on the expression of well-established marker genes. Key markers included: Astrocytes: Aqp4, Gfap, Agt; Microglia: Cx3cr1, Tmem119, P2ry12; Oligodendrocytes: Plp1, Mag, Mog; Monocyte-derived Macrophages: Gpnmb, Spp1, Fabp5; Endothelial cells: Cldn5, Pecam1, Ly6c1; Ependymocytes: Foxj1, Nnat, Rsph1; Neutrophils: Ly6g, S100a8, S100a9; T cells: Cd3d, Cd3e, Nkg7; B cells: Cd79a, Cd79b; Pericytes: Pdgfrb, Vtn; Erythrocytes: Hba-a1, Hba-a2.

Inference of miRNA Activity

miRNA activity was inferred using the miTEA-HiRes (microRNA Target Enrichment Analysis - High Resolution) software(Nielsen and Pedersen 2021), a statistically robust method designed for evaluating miRNA regulatory activity at single-cell and spatial transcriptomics resolution. Mouse 3'untranslated region (3'UTR) sequences were retrieved from Ensembl (release 106). For each cell, genes were ranked in ascending order based on their expression fold-change values between SCI and control groups. miTEA-HiRes employs a minimum HyperGeometric (mHG) test to assess the enrichment of miRNA target genes within the ranked lists. The method relies on a curated miRNA-target interaction set derived from miRTarBase, including only interactions with at least one strong experimental support or two weak experimental supports, ensuring high confidence in predicted regulatory relationships miRNA activity scores were defined as $-\log_{10}$(p-value) × sign(statistic), where p-values were derived from hypergeometric tests. Activity scores were z-score normalized within each cell type. This computational inference approach leverages the principle that increased miRNA activity leads to downregulation of its target genes, resulting in detectable enrichment of miRNA target genes among downregulated transcripts.

Differential Analysis of miRNA Activity

To assess global changes in miRNA regulatory activity following SCI, we performed differential activity analysis comparing injured and uninjured samples. For each miRNA in each cell type, we extracted the inferred activity scores for all cells belonging to that type. Activity scores were compared between injured samples (pooling all post-injury time points) and uninjured controls using the Wilcoxon rank-sum test. miRNAs with $|\log_2 FC| > 0.5$ and adjusted p-value < 0.05 (Bonferroni correction) were considered significantly differentially active. The results are visualized as a volcano plot, with each dot representing a unique miRNA-cell type pair.

Temporal Clustering of miRNA Activity (Mfuzz)

To identify dynamic patterns of miRNA activity across injury time points, temporal clustering was performed using Mfuzz (v2.60.0) (Kumar 2007). The standardized miRNA activity matrix was subjected to fuzzy c-means clustering. The number of clusters ($k = 8$) was selected based on both biological rationale and statistical optimization. Biologically, SCI progression encompasses acute (0.5–3 days), subacute (7–14 days), and chronic (60–90 days) phases, each potentially associated with miRNA upregulation, downregulation, or complex biphasic patterns. Statistically, we evaluated k values from 4 to 10 using average silhouette width, with $k = 8$ yielding the highest value (0.44) and producing clusters with clear, distinct temporal patterns. This choice also enabled consistent cross-cell type comparisons. miRNAs with membership values > 0.5 were assigned to the corresponding trend.

miRNA Target Prediction and Functional Enrichment Analysis

Target genes of differentially active miRNAs were predicted using miRanda (v3.3a) with thresholds: Total_Score ≥ 200 and Tot_Energy ≤ -30 (Clyde 2022). Predictions were intersected with TargetScan (v8.0) and miRDB (v6.0) to enhance reliability(Dogan et al. 2022).

Functional enrichment analysis was conducted using clusterProfiler (v4.6.2) for KEGG pathways and Hallmark gene sets. Terms with an FDR-adjusted p-value < 0.05 were considered significant.

Gene set enrichment analysis (GSEA) was performed using fgsea (v1.24.0) with gene sets from MSigDB (v7.5) (Wang et al. 2024). Gene sets with |NES| > 1.5 and $p < 0.05$ were regarded as significantly enriched.

Construction of miRNA–Target–Pathway Networks

To identify high-confidence miRNA-target interactions, we employed a hierarchical filtering strategy prioritizing experimental evidence and multi-algorithm computational support. First, we retrieved experimentally validated miRNA-target interactions from the miRTarBase database, including only interactions supported by strong experimental evidence. For miRNAs without experimentally validated targets or to expand the network, we performed computational predictions using three independent algorithms: miRanda (v3.3a) with thresholds Total_Score ≥ 200 and Tot_Energy ≤ 30, TargetScan (v8.0) using cumulative weighted context++scores, and miRDB (v6.0) using prediction scores. Additionally, miRWalk binding probabilities were considered. Target genes supported by at least two of these three computational sources (TargetScan, miRDB, miRWalk) were retained for further analysis. After establishing candidate miRNA-target pairs based on experimental validation or multi-algorithm support, we applied an expression correlation filter using our single-cell data. Pearson correlation coefficients were calculated between miRNA activity scores and target gene expression across all cells. Pairs showing significant inverse correlation ($r < -0.2$, adjusted $p < 0.05$) were retained, confirming that the predicted regulatory relationship is active in the SCI context. Finally, networks were manually curated for biological relevance to specific pathways (e.g., INFLAMMATORY_RESPONSE, APOPTOSIS) and visualized using Cytoscape (v3.9.1). Detailed filtering statistics, including numbers of pairs retained at each step, are provided in Supplementary Tables 1–3.

Experimental Validation of miR-130a-3p in Microglial Inflammation

Cell Culture and Treatment

BV-2 murine microglial cells were obtained from the American Type Culture Collection (ATCC) and cultured in DMEM medium supplemented with 10% fetal bovine serum (FBS), 100 U/mL penicillin, and 100 µg/mL streptomycin at 37 °C in a 5% CO_2 atmosphere. Cells were seeded in 6-well plates at a density of 2×10^5 cells per well and allowed to adhere overnight. For inflammation induction, cells were stimulated with lipopolysaccharide (LPS, 100 ng/mL) for 24 h.

miRNA Transfection

miR-130a-3p inhibitor, negative control inhibitor (NC-inhibitor), and corresponding mimics were synthesized by RiboBio (Guangzhou, China). BV-2 cells were transfected at 50% confluence using Lipofectamine 3000 (Invitrogen) according to the manufacturer's protocol. The final concentration of miRNA inhibitor was 50 nM. After 48 h of transfection, cells were treated with LPS (100 ng/mL) for an additional 24 h before analysis.

RNA Extraction and Quantitative Real-Time PCR (qRT-PCR)

Total RNA was extracted from BV-2 cells using TRIzol reagent (Invitrogen) according to the manufacturer's instructions. For miRNA detection, cDNA was synthesized using the Mir-X miRNA First-Strand Synthesis Kit (Takara, Japan). qRT-PCR was performed using TB Green Premix Ex Taq II (Takara) on a LightCycler 480 System (Roche). U6 snRNA was used as an internal control for miRNA normalization. The relative expression levels were calculated using the $2^{-}\Delta\Delta Ct$ method. Primers for miR-130a-3p and U6 were purchased from RiboBio.

Enzyme-Linked Immunosorbent Assay (ELISA)

Culture supernatants from BV-2 cells were collected after LPS stimulation. Concentrations of tumor necrosis factor-alpha (TNF-α) and interleukin-6 (IL-6) were measured using commercial ELISA kits (R&D Systems, Minneapolis, MN, USA) according to the manufacturer's protocols. Each sample was assayed in triplicate, and absorbance was read at 450 nm using a microplate reader (Bio-Rad, Hercules, CA, USA).

Western Blot Analysis

BV-2 cells were lysed in RIPA buffer (Beyotime, China) containing protease inhibitor cocktail. Protein concentrations were determined using the BCA protein assay kit (Thermo Fisher Scientific). Equal amounts of protein (30 µg) were separated by 12% SDS-PAGE and transferred

to PVDF membranes (Millipore). Membranes were blocked with 5% non-fat milk in TBST for 1 h at room temperature and incubated overnight at 4 °C with primary antibodies against TNF-α (1:1000, Abcam), IL-6 (1:1000, Abcam), and GAPDH (1:5000, Cell Signaling Technology). After washing, membranes were incubated with HRP-conjugated secondary antibodies (1:5000, Cell Signaling Technology) for 1 h at room temperature. Protein bands were visualized using enhanced chemiluminescence (ECL) reagent (Millipore) and quantified using ImageJ software.

Experimental Validation of miR-7a-5p in Astrocyte Apoptosis

Cell Culture and Treatment

C8-D1A murine astrocyte cells were obtained from ATCC and cultured in DMEM medium supplemented with 10% FBS, 100 U/mL penicillin, and 100 µg/mL streptomycin at 37 °C in a 5% CO_2 atmosphere. To induce oxidative stress and apoptosis, cells were treated with 200 µM hydrogen peroxide (H_2O_2) for 12 h.

miRNA Transfection

miR-7a-5p mimic, negative control mimic (NC-mimic), and corresponding inhibitors were synthesized by RiboBio. C8-D1A cells were transfected at 50% confluence using Lipofectamine 3000 with a final miRNA mimic concentration of 50 nM. After 48 h of transfection, cells were treated with H_2O_2 (200 µM) for an additional 12 h before analysis.

Cell Viability Assay

Cell viability was assessed using the Cell Counting Kit-8 (CCK-8, Dojindo, Japan). C8-D1A cells were seeded in 96-well plates at a density of 5×10^3 cells per well. After treatment, 10 µL of CCK-8 solution was added to each well and incubated for 2 h at 37 °C. Absorbance was measured at 450 nm using a microplate reader. Cell viability was calculated as (OD_{450}_sample - OD_{450}_blank) / (OD_{450}_control - OD_{450}_blank) × 100%, and expressed as percentage relative to the control group at each time point.

Apoptosis Assay by Flow Cytometry

Apoptosis was detected using the Annexin V-FITC/PI Apoptosis Detection Kit (BD Biosciences) according to the manufacturer's protocol. Briefly, C8-D1A cells were collected, washed twice with cold PBS, and resuspended in 500 µL binding buffer. Cells were then incubated with 5 µL Annexin V-FITC and 5 µL propidium iodide (PI) for 15 min at room temperature in the dark. Apoptotic cells were analyzed using a flow cytometer (BD FACSCanto II) within 1 h. Data were analyzed using FlowJo software (v10.0).

Statistical Analysis

All statistical analyses were performed in R (v4.2.2). Group comparisons were conducted using the non-parametric Mann–Whitney U test, with multiple testing correction via the Bonferroni method. A p-value < 0.05 was considered statistically significant. Data visualization was performed using ggplot2 (v3.4.2) and ComplexHeatmap (v2.14.0).

Result

Construction of Computationally Inferred Single-Cell Transcriptomic Atlas and Cell Type Identification in Spinal Cord Injury Mice

To systematically dissect the dynamic changes in cellular composition following spinal cord injury (SCI), we integrated single-cell transcriptomic data from the GSE189070 dataset, encompassing eight time points: uninjured control and 0.5, 1, 3, 7, 14, 30, 60, and 90 days post-injury. After unified quality control, batch correction, and normalization, a total of 75,183 high-quality cells were retained for unsupervised clustering and cell type annotation. As shown in Fig. 1A, UMAP dimensionality reduction partitioned the cells into 30 transcriptomic clusters. Based on the expression patterns of established marker genes (Fig. 1C), we successfully identified 12 major cell types (Fig. 1B), including: Glial cells: Microglia, Astrocytes, Oligodendrocytes, Ependymocytes; Immune cells: Monocytes, Monocyte-derived Macrophages, Neutrophils, T cells, B cells; Vascular-associated cells: Endothelial cells, Pericytes; Other cells: Erythrocytes. Notably, oligodendrocytes and microglia exhibited the highest cell counts and gene detection numbers (Fig. 1D), suggesting their potential pivotal roles in post-SCI responses. Temporal analysis (Fig. 1E) demonstrated a significant increase in neutrophils and monocyte-derived macrophages during the early injury phase (0.5–3 days), whereas microglia and astrocytes were persistently enriched in the chronic phase (60–90 days), reflecting the dynamic remodeling of immune and glial cell populations after SCI.

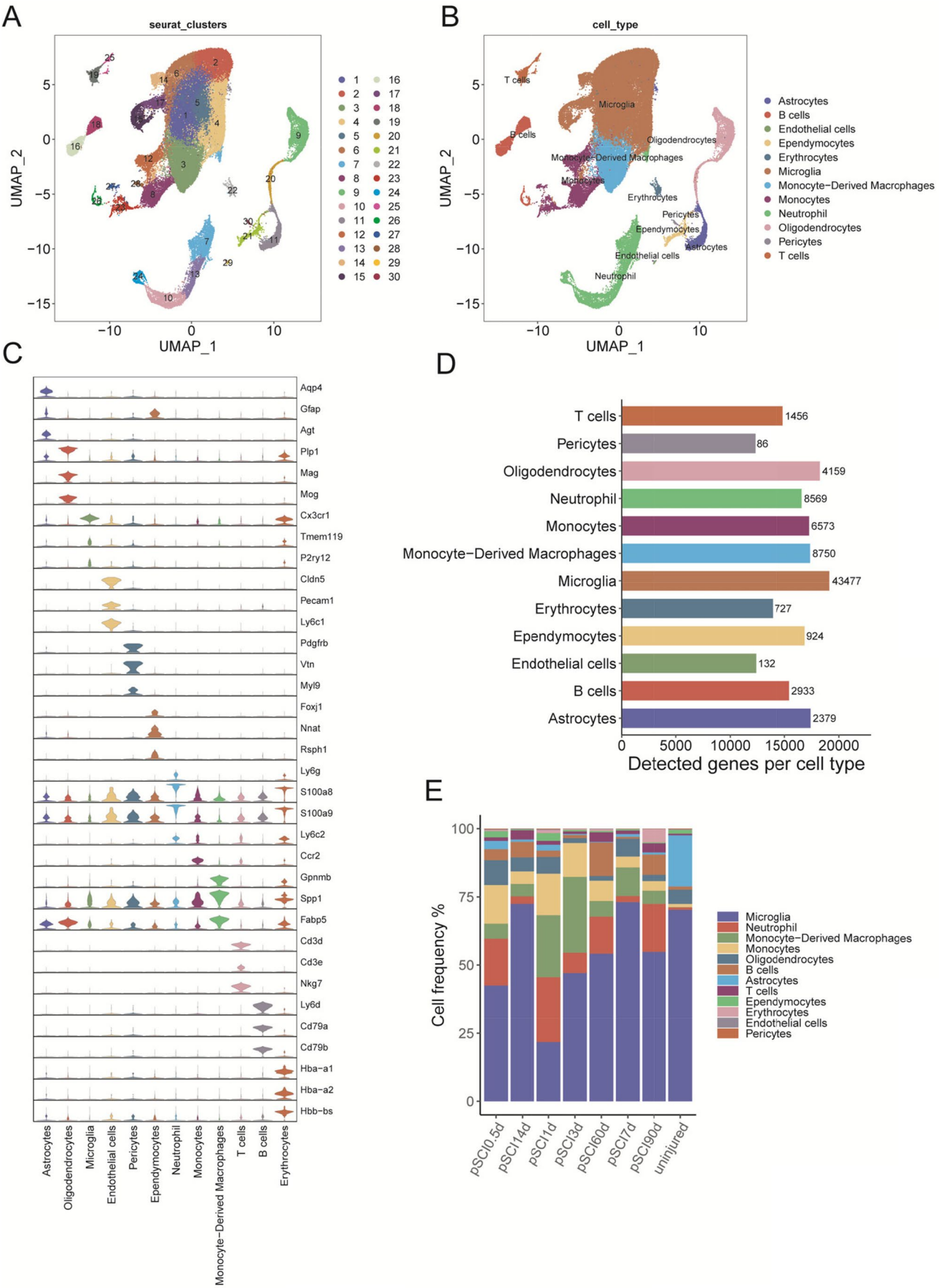
A
seurat_clusters
UMAP_1
UMAP_2
B
cell_type
T cells
Microglia
B cells
Oligodendrocytes
Monocyte−Derived Macrophages
Monocytes
Erythrocytes
Pericytes
Ependymocytes
Astrocytes
Endothelial cells
Neutrophil
Astrocytes
B cells
Endothelial cells
Ependymocytes
Erythrocytes
Microglia
Monocyte−Derived Macrophages
Monocytes
Neutrophil
Oligodendrocytes
Pericytes
T cells
C
Aqp4
Gfap
Agt
Plp1
Mag
Mog
Cx3cr1
Tmem119
P2ry12
Cldn5
Pecam1
Ly6c1
Pdgfrb
Vtn
Myl9
Foxj1
Nnat
Rsph1
Ly6g
S100a8
S100a9
Ly6c2
Ccr2
Gpnmb
Spp1
Fabp5
Cd3d
Cd3e
Nkg7
Ly6d
Cd79a
Cd79b
Hba−a1
Hba−a2
Hbb−bs
Astrocytes
Oligodendrocytes
Microglia
Endothelial cells
Pericytes
Ependymocytes
Neutrophil
Monocytes
Monocyte−Derived Macrophages
T cells
B cells
Erythrocytes
D
T cells 1456
Pericytes 86
Oligodendrocytes 4159
Neutrophil 8569
Monocytes 6573
Monocyte−Derived Macrophages 8750
Microglia 43477
Erythrocytes 727
Ependymocytes 924
Endothelial cells 132
B cells 2933
Astrocytes 2379
Detected genes per cell type
E
Cell frequency %
pSCI0.5d
pSCI14d
pSCI1d
pSCI3d
pSCI60d
pSCI7d
pSCI90d
uninjured
Microglia
Neutrophil
Monocyte−Derived Macrophages
Monocytes
Oligodendrocytes
B cells
Astrocytes
T cells
Ependymocytes
Erythrocytes
Endothelial cells
Pericytes

Fig. 1 Single-cell transcriptomic atlas of spinal cord injury (SCI) in mice. (**A**) UMAP dimensionality reduction plot showing cell clustering results. Different colors represent 30 transcriptional clusters (seurat_clusters). (**B**) UMAP plot after cell type annotation, displaying 12 identified cell types (cell_type). (**C**) Heatmap illustrating the expression intensity and specificity of marker genes across 12 cell types. Color intensity indicates normalized expression levels. (**D**) Bar chart showing the number of detected genes per cell type. (**E**) Heatmap depicting the relative frequency of each cell type across time points. Color represents cell frequency (%)

Construction of Computationally Inferred Single-Cell miRNA Activity Atlas in Spinal Cord Injury

To investigate the regulatory potential of miRNAs at single-cell resolution following spinal cord injury (SCI), we employed a motif enrichment-based computational approach to infer miRNA activity across 12 major cell types, thereby constructing the first dynamic atlas of computationally inferred miRNA regulatory activity throughout SCI progression. As shown in Fig. 2A, we revealed that a subset of miRNAs exhibited coordinated activity changes across multiple cell types. Specifically, mmu-miR-200a-3p, mmu-miR-132-3p, and mmu-miR-129-5p showed consistently decreased activity following injury across various cell populations. In contrast, mmu-miR-488-3p, mmu-miR-300-3p, and mmu-miR-16b-3p displayed universally increased activity, indicating their potential roles as common regulatory factors in the post-SCI microenvironment. To systematically identify miRNAs with significantly altered regulatory activity following SCI, we performed differential activity analysis comparing injured and uninjured samples within each cell type. The volcano plot summarizes the comparative results for all miRNA–cell type pairs (Fig. 2B). As shown in Fig. 2C, we identified cell type-specific miRNAs with the highest activity in each population. For instance, mmu-miR-3110-5p was specifically enriched in astrocytes, while mmu-miR-92a-3p exhibited high activity in endothelial cells. In microglia, mmu-miR-5097 and mmu-miR-188-3p showed increased activity specifically following injury, whereas miR-208b-3p displayed elevated activity in monocyte-derived macrophages. Conversely, mmu-miR-191-5p showed significantly reduced activity in oligodendrocytes, and mmu-miR-466 g was decreased in neutrophils. These cell type-specific miRNA activity patterns suggest their potential involvement in maintaining cellular identity and regulating functional states in response to SCI.

To validate the reliability of our computationally inferred miRNA activity patterns, we performed an orthogonal comparison using an independent bulk miRNA sequencing dataset (GSE90452). This dataset contains miRNA expression profiles from spinal cord tissues of control and SCI mice, allowing us to directly measure actual miRNA abundance changes following injury. As shown in Supplementary Fig. 1, miRNAs that were inferred to have increased activity in our single-cell atlas (e.g., mmu-miR-488-3p, mmu-miR-300-3p, and mmu-miR-16b-3p) consistently exhibited significantly higher expression levels in SCI samples compared to controls in the independent dataset. Conversely, miRNAs with inferred decreased activity (e.g., mmu-miR-200a-3p, mmu-miR-132-3p, and mmu-miR-129-5p) showed correspondingly reduced expression in SCI samples. This concordance between computationally inferred miRNA activity and experimentally measured miRNA expression in an independent cohort provides critical orthogonal validation of our analytical approach, supporting the biological plausibility of the inferred miRNA activity atlas.

Dynamic miRNA Activity and Functional Regulation in Microglia After Spinal Cord Injury

Microglia, as resident immune cells of the central nervous system, undergo significant phenotypic and functional remodeling after SCI, transitioning from a pro-inflammatory "M1-like" to a pro-repair "M2-like" state, which critically influences the balance between neuroinflammation and regeneration. To elucidate the miRNA regulatory mechanisms in microglia during injury progression, we performed temporal activity trend analysis and functional enrichment studies. Mfuzz trend analysis identified eight dynamic miRNA activity patterns in microglia (Fig. 3A). Trends such as Trend1 (early upregulation), Trend2 (sustained upregulation), and Trend4 (late downregulation) were notably associated with inflammatory and repair phases, suggesting that different miRNAs may exert regulatory functions at distinct injury stages. Functional enrichment analysis of target genes of differentially active miRNAs revealed significant enrichment in Hallmark pathways including TNFA_SIGNALING_VIA_NFKB, INFLAMMATORY_RESPONSE, IL6_JAK_STAT3_SIGNALING, and COMPLEMENT, as well as pathways related to APOPTOSIS and OXIDATIVE_PHOSPHORYLATION (Fig. 3B). KEGG enrichment analysis further corroborated these findings, showing significant enrichment in classical inflammatory pathways such as TOLL_LIKE_RECEPTOR_SIGNALING_PATHWAY,

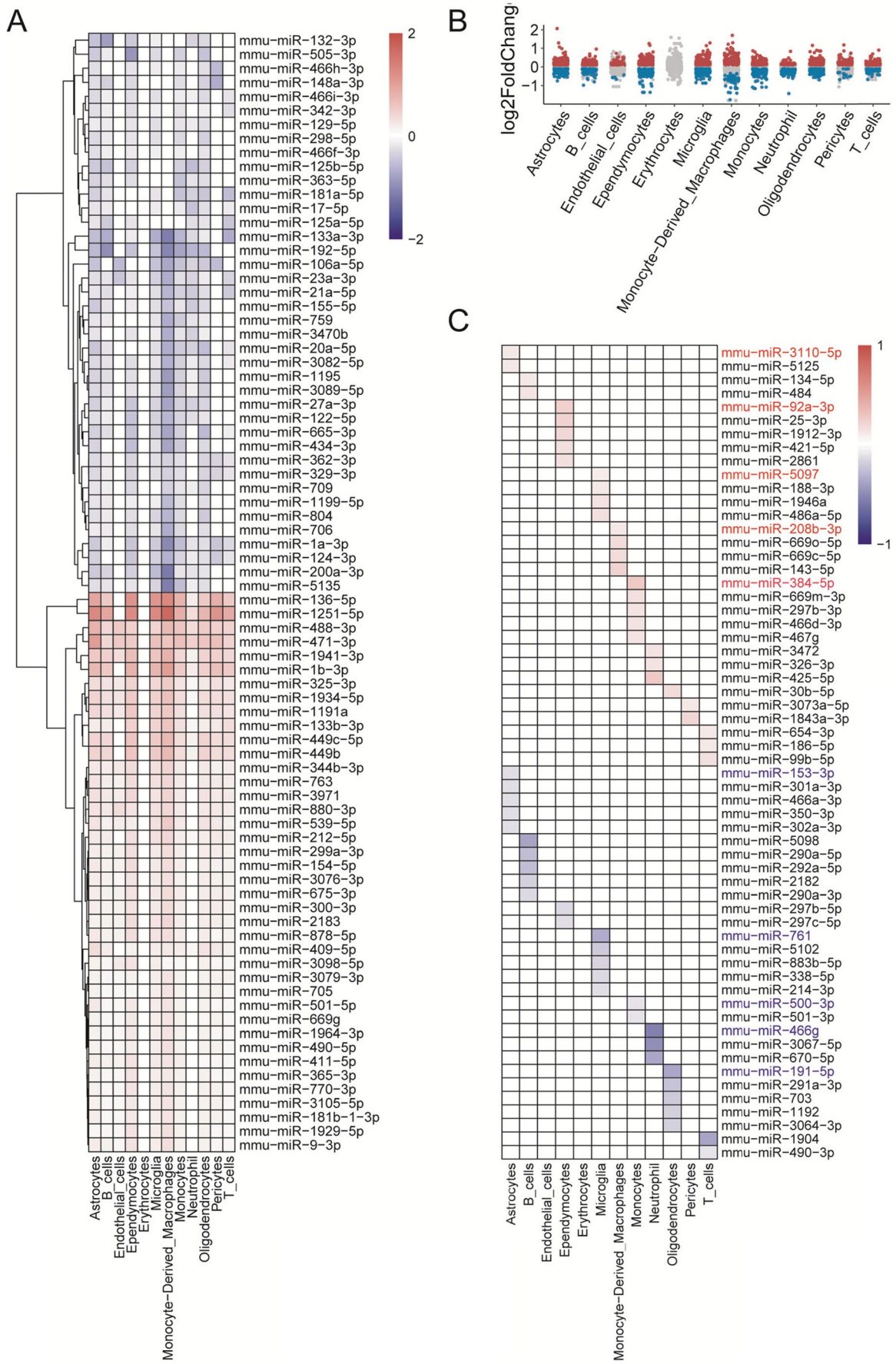
A
mmu-miR-132-3p
mmu-miR-505-3p
mmu-miR-466h-3p
mmu-miR-148a-3p
mmu-miR-466i-3p
mmu-miR-342-3p
mmu-miR-129-5p
mmu-miR-298-5p
mmu-miR-466f-3p
mmu-miR-125b-5p
mmu-miR-363-5p
mmu-miR-181a-5p
mmu-miR-17-5p
mmu-miR-125a-5p
mmu-miR-133a-3p
mmu-miR-192-5p
mmu-miR-106a-5p
mmu-miR-23a-3p
mmu-miR-21a-5p
mmu-miR-155-5p
mmu-miR-759
mmu-miR-3470b
mmu-miR-20a-5p
mmu-miR-3082-5p
mmu-miR-1195
mmu-miR-3089-5p
mmu-miR-27a-3p
mmu-miR-122-5p
mmu-miR-665-3p
mmu-miR-434-3p
mmu-miR-362-3p
mmu-miR-329-3p
mmu-miR-709
mmu-miR-1199-5p
mmu-miR-804
mmu-miR-706
mmu-miR-1a-3p
mmu-miR-124-3p
mmu-miR-200a-3p
mmu-miR-5135
mmu-miR-136-5p
mmu-miR-1251-5p
mmu-miR-488-3p
mmu-miR-471-3p
mmu-miR-1941-3p
mmu-miR-1b-3p
mmu-miR-325-3p
mmu-miR-1934-5p
mmu-miR-1191a
mmu-miR-133b-3p
mmu-miR-449c-5p
mmu-miR-449b
mmu-miR-344b-3p
mmu-miR-763
mmu-miR-3971
mmu-miR-880-3p
mmu-miR-539-5p
mmu-miR-212-5p
mmu-miR-299a-3p
mmu-miR-154-5p
mmu-miR-3076-3p
mmu-miR-675-3p
mmu-miR-300-3p
mmu-miR-2183
mmu-miR-878-5p
mmu-miR-409-5p
mmu-miR-3098-5p
mmu-miR-3079-3p
mmu-miR-705
mmu-miR-501-5p
mmu-miR-669g
mmu-miR-1964-3p
mmu-miR-490-5p
mmu-miR-411-5p
mmu-miR-365-3p
mmu-miR-770-3p
mmu-miR-3105-5p
mmu-miR-181b-1-3p
mmu-miR-1929-5p
mmu-miR-9-3p
2
0
−2
Astrocytes
B_cells
Endothelial_cells
Ependymocytes
Erythrocytes
Microglia
Monocyte−Derived_Macrophages
Monocytes
Neutrophil
Oligodendrocytes
Pericytes
T_cells
B
log2FoldChang
2
1
0
−1
Astrocytes
B_cells
Endothelial_cells
Ependymocytes
Erythrocytes
Microglia
Monocyte−Derived_Macrophages
Monocytes
Neutrophil
Oligodendrocytes
Pericytes
T_cells
C
mmu-miR-3110-5p
mmu-miR-5125
mmu-miR-134-5p
mmu-miR-484
mmu-miR-92a-3p
mmu-miR-25-3p
mmu-miR-1912-3p
mmu-miR-421-5p
mmu-miR-2861
mmu-miR-5097
mmu-miR-188-3p
mmu-miR-1946a
mmu-miR-486a-5p
mmu-miR-208b-3p
mmu-miR-669o-5p
mmu-miR-669c-5p
mmu-miR-143-5p
mmu-miR-384-5p
mmu-miR-669m-3p
mmu-miR-297b-3p
mmu-miR-466d-3p
mmu-miR-467g
mmu-miR-3472
mmu-miR-326-3p
mmu-miR-425-5p
mmu-miR-30b-5p
mmu-miR-3073a-5p
mmu-miR-1843a-3p
mmu-miR-654-3p
mmu-miR-186-5p
mmu-miR-99b-5p
mmu-miR-153-3p
mmu-miR-301a-3p
mmu-miR-466a-3p
mmu-miR-350-3p
mmu-miR-302a-3p
mmu-miR-5098
mmu-miR-290a-5p
mmu-miR-292a-5p
mmu-miR-2182
mmu-miR-290a-3p
mmu-miR-297b-5p
mmu-miR-297c-5p
mmu-miR-761
mmu-miR-5102
mmu-miR-883b-5p
mmu-miR-338-5p
mmu-miR-214-3p
mmu-miR-500-3p
mmu-miR-501-3p
mmu-miR-466g
mmu-miR-3067-5p
mmu-miR-670-5p
mmu-miR-191-5p
mmu-miR-291a-3p
mmu-miR-703
mmu-miR-1192
mmu-miR-3064-3p
mmu-miR-1904
mmu-miR-490-3p
1
−1
Astrocytes
B_cells
Endothelial_cells
Ependymocytes
Erythrocytes
Microglia
Monocyte−Derived_Macrophages
Monocytes
Neutrophil
Oligodendrocytes
Pericytes
T_cells

Fig. 2 Construction of computationally inferred single-cell miRNA activity atlas in spinal cord injury. (**A**) Heatmap showing miRNAs with commonly upregulated (red) or downregulated (blue) activity across all cell types. (**B**) Volcano plot summarizing changes in inferred miRNA activity following SCI. For each miRNA in each cell type, we compared activity scores between all injured samples (pooled across post-injury time points) and uninjured controls. Red dots indicate miRNAs with significantly increased activity in injured samples ($|\log_2 FC| > 0.5$, adjusted $p < 0.05$), blue dots indicate miRNAs with significantly decreased activity, and gray dots indicate miRNAs with no significant change. Each dot represents a unique miRNA-cell type pair. (C) Heatmap displaying the top cell type-specific miRNAs in terms of activity across 12 cell types. Color indicates $\log_2$FoldChange values

NF-KB_SIGNALING, and CHEMOKINE_SIGNALING_PATHWAY (Fig. 3C), indicating that miRNAs regulate microglial function through inflammatory networks. To validate these regulatory inferences at the transcriptional level, we performed differential expression analysis on microglial genes and conducted independent KEGG enrichment. Notably, the pathways enriched among differentially expressed genes (Fig. 3D) were highly concordant with those identified from miRNA target analysis, both converging on key inflammatory and immune-related processes. This consistency was further reinforced by Gene Set Enrichment Analysis (GSEA), which confirmed significant upregulation of gene sets associated with inflammatory responses and cytokine signaling in microglia following injury (Fig. 3E). This alignment suggests that the dynamic changes in miRNA activity we observed are functionally relevant, actively shaping the microglial transcriptome and driving the inflammatory phenotype that characterizes the cellular response to spinal cord injury.

Dynamic miRNA Activity and Functional Regulation in Monocyte-Derived Macrophages After Spinal Cord Injury

Monocyte-derived macrophages play a crucial role in inflammatory responses and tissue repair following SCI. To systematically investigate miRNA regulatory mechanisms in these cells during injury progression, we conducted temporal activity trend analysis and functional enrichment studies. Mfuzz analysis identified eight dynamic miRNA activity trends in macrophages (Fig. 4A). Among these, Trend1 (acute rapid upregulation) and Trend3 (subacute sustained upregulation) were associated with early inflammatory activation, whereas Trend7 (chronic downregulation) may relate to inflammation resolution or repair phases, reflecting the diversity of miRNA regulation across different injury stages. KEGG and Hallmark pathway enrichment analyses of target genes from differentially active miRNAs showed significant enrichment in classical inflammatory and immune pathways, including TOLL_LIKE_RECEPTOR_SIGNALING_PATHWAY, CHEMOKINE_SIGNALING_PATHWAY, CYTOKINE_CYTOKINE_RECEPTOR_INTERACTION, INFLAMMATORY_RESPONSE, and TNFA_SIGNALING_VIA_NFKB (Fig. 4B, C), indicating that miRNAs participate in macrophage functional regulation through inflammatory networks. Notably, metabolic pathways such as OXIDATIVE_PHOSPHORYLATION and GLYCOLYSIS were also significantly enriched, suggesting potential metabolic reprogramming in macrophages during injury. To validate these regulatory inferences at the transcriptional level and assess global pathway alterations, we performed Gene Set Enrichment Analysis (GSEA) on the transcriptomic profiles of monocyte-derived macrophages after SCI. Figure 4D presents GSEA plots demonstrating significant enrichment of key inflammation-related gene sets. Specifically, the HALLMARK_INFLAMMATORY_RESPONSE gene set was markedly enriched in macrophages following injury, confirming robust activation of inflammatory programs. Additionally, the HALLMARK_TNFA_SIGNALING_VIA_NFKB pathway showed strong enrichment, consistent with the central role of TNF-α/NF-κB signaling in macrophage activation. Enrichment of the HALLMARK_IL6_JAK_STAT3_SIGNALING pathway further supported the involvement of cytokine-mediated signaling cascades. These GSEA results provide orthogonal validation of the pathway enrichments identified from miRNA target analysis, confirming that the dynamic changes in miRNA activity we observed are functionally relevant and actively shape the inflammatory phenotype of macrophages following spinal cord injury.

miRNA–Target–Inflammatory Pathway Regulatory Network in Microglia and Macrophages

To elucidate the cooperative regulatory mechanisms of microglia and macrophages in SCI-associated inflammatory responses, we focused on the Trend7 miRNAs from microglia (90 miRNAs) and the Trend4 miRNAs from macrophages (64 miRNAs), both of which were closely associated with post-injury inflammatory processes. Comparative analysis identified 38 common differentially active miRNAs between the two cell types (Fig. 5A–C), suggesting potential cooperative regulation across immune cells. We then

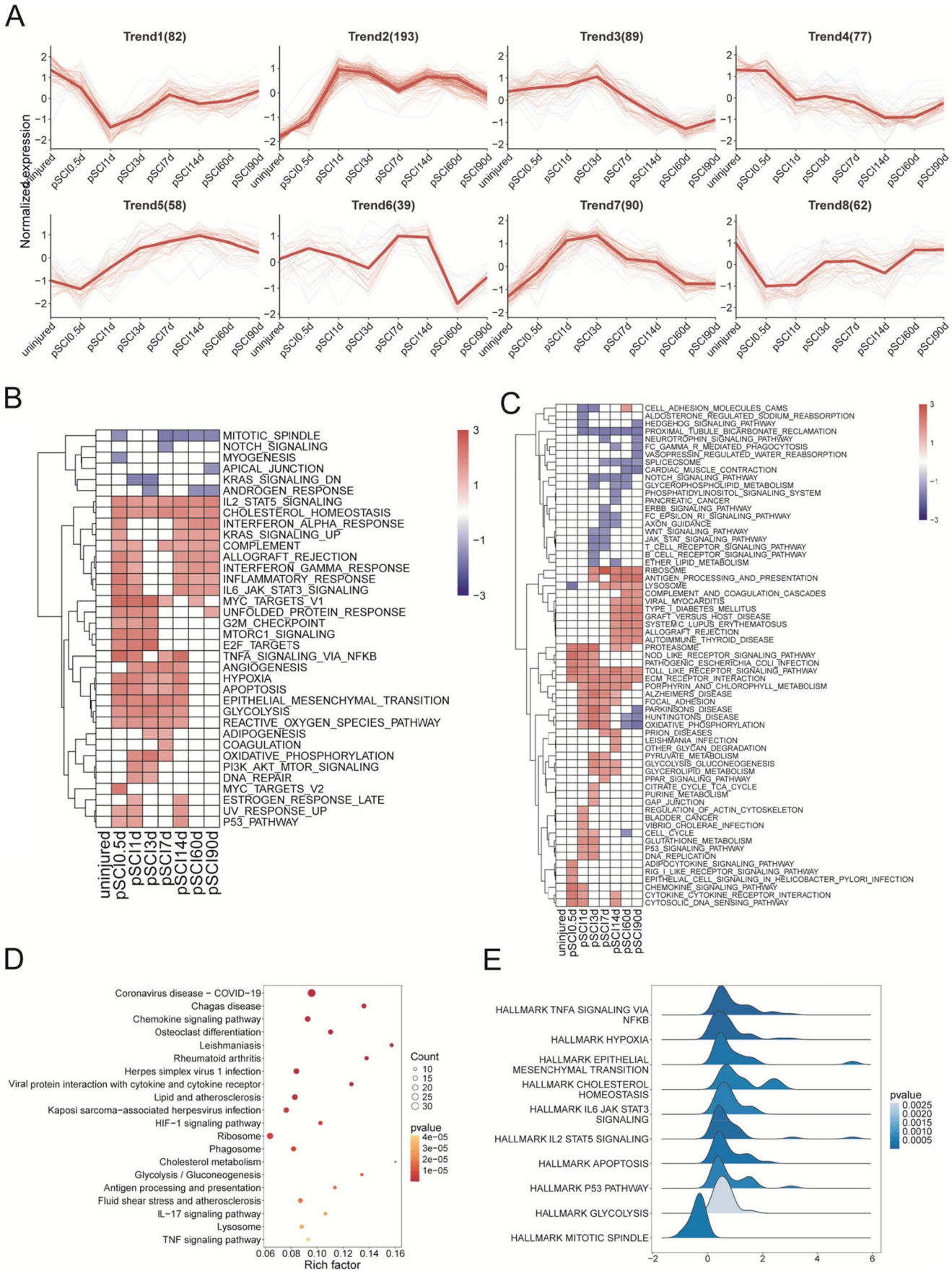
A
Trend1(82)
Trend2(193)
Trend3(89)
Trend4(77)
Trend5(58)
Trend6(39)
Trend7(90)
Trend8(62)
Normalized expression
uninjured
pSCI0.5d
pSCI1d
pSCI3d
pSCI7d
pSCI14d
pSCI60d
pSCI90d
B
MITOTIC_SPINDLE
NOTCH_SIGNALING
MYOGENESIS
APICAL_JUNCTION
KRAS_SIGNALING_DN
ANDROGEN_RESPONSE
IL2_STAT5_SIGNALING
CHOLESTEROL_HOMEOSTASIS
INTERFERON_ALPHA_RESPONSE
KRAS_SIGNALING_UP
COMPLEMENT
ALLOGRAFT_REJECTION
INTERFERON_GAMMA_RESPONSE
INFLAMMATORY_RESPONSE
IL6_JAK_STAT3_SIGNALING
MYC_TARGETS_V1
UNFOLDED_PROTEIN_RESPONSE
G2M_CHECKPOINT
MTORC1_SIGNALING
E2F_TARGETS
TNFA_SIGNALING_VIA_NFKB
ANGIOGENESIS
HYPOXIA
APOPTOSIS
EPITHELIAL_MESENCHYMAL_TRANSITION
GLYCOLYSIS
REACTIVE_OXYGEN_SPECIES_PATHWAY
ADIPOGENESIS
COAGULATION
OXIDATIVE_PHOSPHORYLATION
PI3K_AKT_MTOR_SIGNALING
DNA_REPAIR
MYC_TARGETS_V2
ESTROGEN_RESPONSE_LATE
UV_RESPONSE_UP
P53_PATHWAY
C
CELL_ADHESION_MOLECULES_CAMS
ALDOSTERONE_REGULATED_SODIUM_REABSORPTION
HEDGEHOG_SIGNALING_PATHWAY
PROXIMAL_TUBULE_BICARBONATE_RECLAMATION
NEUROTROPHIN_SIGNALING_PATHWAY
FC_GAMMA_R_MEDIATED_PHAGOCYTOSIS
VASOPRESSIN_REGULATED_WATER_REABSORPTION
SPLICEOSOME
CARDIAC_MUSCLE_CONTRACTION
NOTCH_SIGNALING_PATHWAY
GLYCEROPHOSPHOLIPID_METABOLISM
PHOSPHATIDYLINOSITOL_SIGNALING_SYSTEM
PANCREATIC_CANCER
ERBB_SIGNALING_PATHWAY
FC_EPSILON_RI_SIGNALING_PATHWAY
AXON_GUIDANCE
WNT_SIGNALING_PATHWAY
JAK_STAT_SIGNALING_PATHWAY
T_CELL_RECEPTOR_SIGNALING_PATHWAY
B_CELL_RECEPTOR_SIGNALING_PATHWAY
ETHER_LIPID_METABOLISM
RIBOSOME
ANTIGEN_PROCESSING_AND_PRESENTATION
LYSOSOME
COMPLEMENT_AND_COAGULATION_CASCADES
VIRAL_MYOCARDITIS
TYPE_I_DIABETES_MELLITUS
GRAFT_VERSUS_HOST_DISEASE
SYSTEMIC_LUPUS_ERYTHEMATOSUS
ALLOGRAFT_REJECTION
AUTOIMMUNE_THYROID_DISEASE
PROTEASOME
NOD_LIKE_RECEPTOR_SIGNALING_PATHWAY
PATHOGENIC_ESCHERICHIA_COLI_INFECTION
TOLL_LIKE_RECEPTOR_SIGNALING_PATHWAY
ECM_RECEPTOR_INTERACTION
PORPHYRIN_AND_CHLOROPHYLL_METABOLISM
ALZHEIMERS_DISEASE
FOCAL_ADHESION
PARKINSONS_DISEASE
HUNTINGTONS_DISEASE
OXIDATIVE_PHOSPHORYLATION
PRION_DISEASES
LEISHMANIA_INFECTION
OTHER_GLYCAN_DEGRADATION
PYRUVATE_METABOLISM
GLYCOLYSIS_GLUCONEOGENESIS
GLYCEROLIPID_METABOLISM
PPAR_SIGNALING_PATHWAY
CITRATE_CYCLE_TCA_CYCLE
PURINE_METABOLISM
GAP_JUNCTION
REGULATION_OF_ACTIN_CYTOSKELETON
BLADDER_CANCER
VIBRIO_CHOLERAE_INFECTION
CELL_CYCLE
GLUTATHIONE_METABOLISM
P53_SIGNALING_PATHWAY
DNA_REPLICATION
ADIPOCYTOKINE_SIGNALING_PATHWAY
RIG_I_LIKE_RECEPTOR_SIGNALING_PATHWAY
EPITHELIAL_CELL_SIGNALING_IN_HELICOBACTER_PYLORI_INFECTION
CHEMOKINE_SIGNALING_PATHWAY
CYTOKINE_CYTOKINE_RECEPTOR_INTERACTION
CYTOSOLIC_DNA_SENSING_PATHWAY
D
Coronavirus disease - COVID-19
Chagas disease
Chemokine signaling pathway
Osteoclast differentiation
Leishmaniasis
Rheumatoid arthritis
Herpes simplex virus 1 infection
Viral protein interaction with cytokine and cytokine receptor
Lipid and atherosclerosis
Kaposi sarcoma-associated herpesvirus infection
HIF-1 signaling pathway
Ribosome
Phagosome
Cholesterol metabolism
Glycolysis / Gluconeogenesis
Antigen processing and presentation
Fluid shear stress and atherosclerosis
IL-17 signaling pathway
Lysosome
TNF signaling pathway
Rich factor
Count
pvalue
E
HALLMARK TNFA SIGNALING VIA NFKB
HALLMARK HYPOXIA
HALLMARK EPITHELIAL MESENCHYMAL TRANSITION
HALLMARK CHOLESTEROL HOMEOSTASIS
HALLMARK IL6 JAK STAT3 SIGNALING
HALLMARK IL2 STAT5 SIGNALING
HALLMARK APOPTOSIS
HALLMARK P53 PATHWAY
HALLMARK GLYCOLYSIS
HALLMARK MITOTIC SPINDLE
pvalue

Fig. 3 Dynamic miRNA activity and functional regulation in microglia after spinal cord injury. (**A**) Mfuzz trend analysis of miRNA activity changes in microglia, identifying 8 dynamic trends. Numbers on the right indicate the number of miRNAs in each trend. (**B**) Heatmap of Hallmark pathway enrichment analysis for miRNA target genes. Color represents normalized enrichment score (NES). (**C**) Heatmap of KEGG pathway enrichment analysis for miRNA target genes. Color represents NES. (**D**) KEGG pathway enrichment analysis of differentially expressed genes (DEGs) in microglia following SCI. (**E**) Gene set enrichment analysis (GSEA) plots depicting significant enrichment of inflammation-related gene sets in microglia after injury

plotted heatmaps showing the dynamic expression of these common miRNAs in microglia (Fig. 5D) and macrophages (Fig. 5E). The results revealed that miRNAs such as mmu-miR-130a-3p, mmu-miR-27b-3p, and mmu-miR-223-3p were significantly upregulated during early injury and maintained high activity thereafter, indicating their critical roles in initiating and sustaining inflammation. KEGG pathway enrichment analysis further demonstrated that target genes of these common miRNAs were significantly enriched in inflammation- and immune-related pathways, including PI3K-Akt signaling pathway, MAPK signaling pathway, T cell receptor signaling pathway, and FoxO signaling pathway (Fig. 5F), reinforcing the functional relevance of these miRNAs in regulating SCI-related inflammatory responses. Finally, we constructed an miRNA–target–inflammatory pathway (INFLAMMATORY_RESPONSE) interaction network (Fig. 5G), with red nodes representing miRNAs and blue nodes representing target genes. Network analysis revealed that multiple common miRNAs (e.g., mmu-miR-27b-3p, mmu-miR-130a-3p) targeted key inflammatory genes such as Lif, Clec5a, Csf1, Tnfrsf1b, and Il18rap. These genes are broadly involved in cytokine signaling, inflammatory mediator release, and immune cell activation, indicating that this network plays a crucial role in coordinating the inflammatory responses of microglia and macrophages.

Mechanisms of miRNA-Mediated Apoptotic Pathway Regulation in Astrocytes

The significant reduction in astrocyte numbers after SCI is largely attributed to programmed cell death (apoptosis). To investigate the role of miRNAs in regulating astrocyte apoptosis, we performed systematic activity trend analysis and functional network construction. Mfuzz analysis identified eight dynamic miRNA activity patterns in astrocytes (Fig. 6A). Among these, Trend4 (84 miRNAs) and Trend5 (60 miRNAs) were significantly downregulated in the late injury phase, potentially associated with apoptosis inhibition or cell survival, whereas Trend8 (117 miRNAs) showed sustained upregulation during mid-to-late injury stages, possibly promoting apoptosis. GSEA functional enrichment analysis of target genes from differentially active miRNAs revealed significant enrichment in pathways related to apoptosis and inflammation, including APOPTOSIS, P53_PATHWAY, TNFA_SIGNALING_VIA_NFKB, and INFLAMMATORY_RESPONSE (Fig. 6B), suggesting that miRNAs influence astrocyte survival and death by regulating these pathways. igure 6 C presents the miRNA–target–apoptosis pathway (APOPTOSIS) interaction network. This network reveals that miRNAs such as mmu-miR-7a-5p, mmu-miR-124-3p, and mmu-miR-15b-5p target key apoptosis-related genes, including Casp3, Bcl2l1, Bcl2l11, Sod2, Fas, and Tnfsf10. These interactions form dense regulatory modules that collectively coordinate the apoptotic response in astrocytes following injury. Notably, multiple miRNAs converge on the same target genes (e.g., Casp3 is targeted by miR-7a-5p, miR-124-3p, and miR-15b-5p), suggesting cooperative or redundant regulatory mechanisms. Figure 6D displays the miRNA–target–P53 pathway interaction network in astrocytes. This network identifies miRNAs that potentially modulate the P53 signaling cascade, including mmu-miR-7a-5p, mmu-miR-124-3p, and mmu-miR-15b-5p, which target P53 pathway components such as Mdm2, Pmaip1 (Noxa), Bbc3 (Puma), and Cdkn1a (p21). The convergence of multiple miRNAs on both apoptosis and P53 pathways suggests a coordinated regulatory program governing astrocyte stress responses. Figure 6E shows the temporal activity patterns of key apoptosis-regulating miRNAs in astrocytes. Figure 6F depicts the temporal activity patterns of key P53 pathway-regulating miRNAs in astrocytes.

Experimental Validation of miR-130a-3p Pro-inflammatory Function in Microglia Cells

To experimentally validate the computationally predicted roles of miRNAs in microglial inflammation, we focused on miR-130a-3p, one of the 38 common differentially active miRNAs identified in both microglia and macrophages,

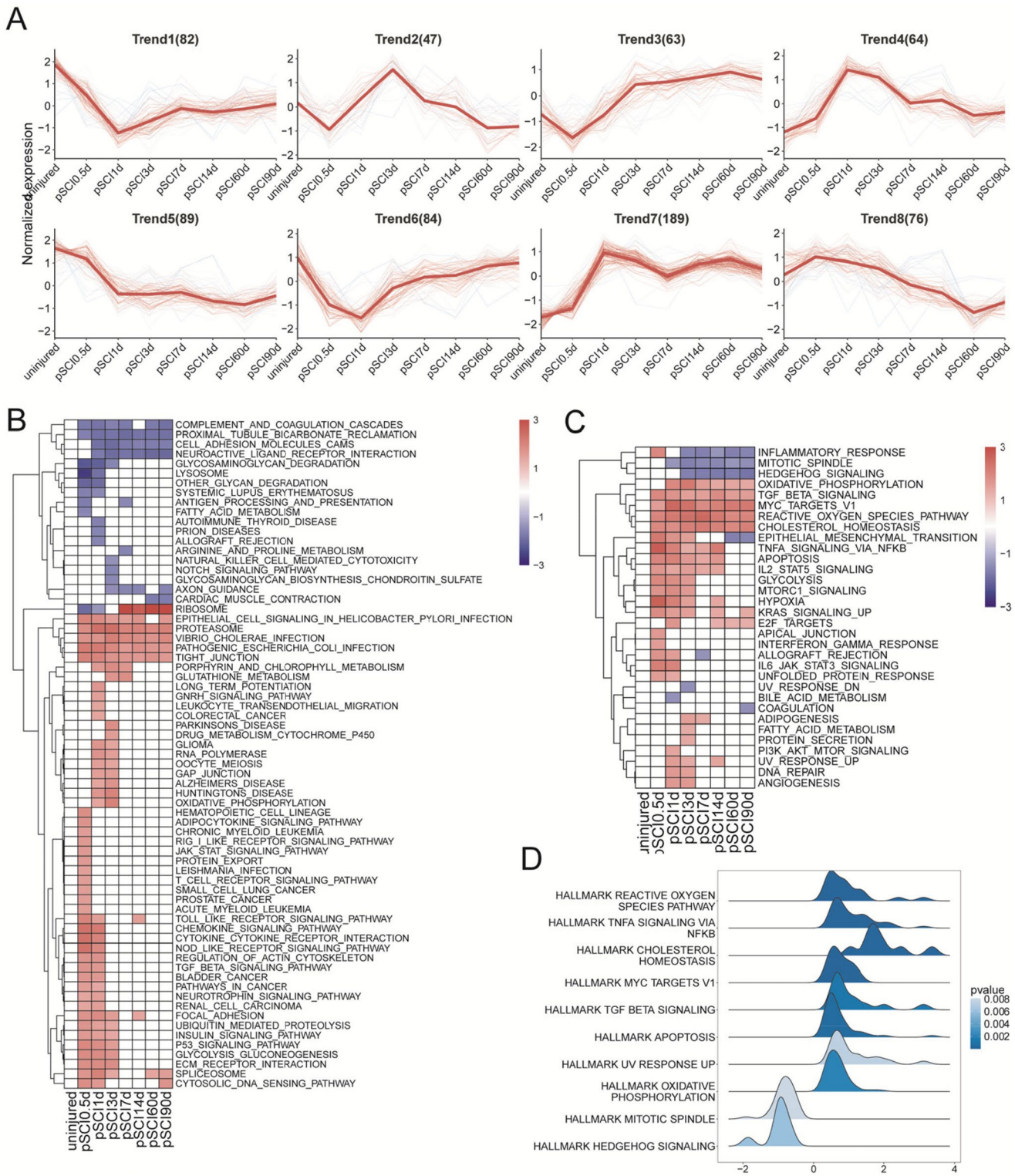

Fig. 4 Dynamic miRNA activity and functional regulation in monocyte-derived macrophages after spinal cord injury. (**A**) Mfuzz trend analysis of miRNA activity changes in macrophages, identifying 8 dynamic trends. Numbers on the right indicate the number of miRNAs in each trend. (**B**) Heatmap of KEGG pathway enrichment analysis for miRNA target genes. Color represents NES. (**C**) Heatmap of Hallmark pathway enrichment analysis for miRNA target genes. Color represents NES. (**D**) Gene set enrichment analysis (GSEA) plots depicting significant enrichment of inflammation-related gene sets in monocyte-derived macrophages after spinal cord injury

and examined its functional role in LPS-stimulated BV-2 microglial cells. qRT-PCR analysis confirmed that LPS stimulation (100 ng/mL, 24 h) significantly upregulated miR-130a-3p expression in BV-2 cells compared to control ($p < 0.01$). This upregulation was effectively reversed by transfection with miR-130a-3p inhibitor, while negative control inhibitor (NC-inhibitor) had no significant effect (Fig. 7A). To assess the functional consequences of miR-130a-3p modulation, we measured the secretion of pro-inflammatory cytokines. ELISA assays demonstrated that LPS stimulation markedly increased TNF-α and IL-6 secretion in culture supernatants ($p < 0.001$). Transfection with miR-130a-3p inhibitor significantly attenuated LPS-induced TNF-α and IL-6 secretion ($p < 0.01$), whereas NC-inhibitor showed no effect (Fig. 7B, C). Consistently, Western blot analysis revealed that miR-130a-3p inhibition significantly reduced the protein levels of TNF-α and IL-6 in LPS-stimulated BV-2 cells (Fig. 7D-F). These results provide direct experimental evidence that miR-130a-3p promotes microglial inflammation, supporting our computational prediction that this miRNA functions as a pro-inflammatory regulator in microglia following SCI.

Experimental Validation of miR-7a-5p Anti-Apoptotic Function in Astrocytes

Our computational network analysis predicted that miR-7a-5p may regulate apoptosis in astrocytes by targeting key apoptotic genes including Casp3. To experimentally validate this prediction, we examined the functional role of miR-7a-5p in H_2O_2-induced oxidative stress and apoptosis in C8-D1A astrocyte cells. First, we confirmed that H_2O_2 treatment (200 μM, 12 h) significantly downregulated miR-7a-5p expression in C8-D1A cells ($p < 0.01$), and miR-7a-5p expression was enhanced by transfection with miR-7a-5p mimic (Fig. 8A). CCK-8 assay showed that H_2O_2 treatment significantly reduced astrocyte viability in a time-dependent manner. Transfection with miR-7a-5p mimic significantly attenuated H_2O_2 -induced cell death at 24, 48 and 72 h (Fig. 8B). Flow cytometry analysis using Annexin V/PI staining demonstrated that H_2O_2 treatment significantly increased the apoptosis rate of C8-D1A cells ($p < 0.001$). Consistent with the viability results, miR-7a-5p mimic transfection significantly attenuated H_2O_2 -induced apoptosis ($p < 0.01$), as evidenced by an increased percentage of Annexin V-positive cells (Fig. 8C, D). To investigate the molecular mechanism, we examined cleaved caspase-3 levels by Western blot. H_2O_2 treatment markedly increased cleaved caspase-3 protein expression ($p < 0.001$), indicating activation of the apoptotic cascade. miR-7a-5p mimic transfection significantly reduced cleaved caspase-3 levels in H_2O_2-treated cells ($p < 0.01$), consistent with its anti-apoptotic function (Fig. 8E, F). These results provide direct experimental validation that miR-7a-5p promotes astrocyte apoptosis under oxidative stress conditions, confirming our computational prediction from the network analysis.

Discussion

Single-cell RNA sequencing (scRNA-seq) has emerged as a powerful tool for resolving cellular heterogeneity and molecular dynamics following spinal cord injury (SCI) (Tansley et al. 2022, Yao et al. 2022). Numerous studies have utilized this technology to characterize changes in various cell subpopulations post-injury, such as the phenotypic switching of microglia and macrophages, reactive astrogliosis, and the damage and regeneration of oligodendrocytes (Saraswathy et al. 2024, Cao et al. 2022). In this study, using samples from eight time points in the GSE189070 dataset, we systematically mapped the dynamic changes of 12 major cell types after SCI. Our findings further confirm the spatiotemporal pattern of rapid immune cell recruitment—particularly neutrophils and monocyte-derived macrophages—in the early injury phase, and the persistent enrichment of neuroglial cells (microglia and astrocytes) during the chronic phase. These observations align with previously reported temporal features of immune and inflammatory responses in SCI, supporting a dual-phase injury response model characterized by "early inflammation clearance and late glial remodeling" (Cavalcanti et al. 2025, Lai et al. 2024).

A key methodological contribution of this study is the inference of miRNA regulatory activity at single-cell resolution using miTEA-HiRes. Investigating miRNA function at the single-cell level has long presented technical challenges, primarily because conventional scRNA-seq platforms are inefficient at capturing miRNAs lacking poly-A tails (Olgun et al. 2022). Motif enrichment-based analytical approaches provide new avenues for indirectly inferring miRNA activity from transcriptomic data (Nielsen and Pedersen 2021). Adopting this methodology, we constructed the first dynamic single-cell miRNA activity atlas

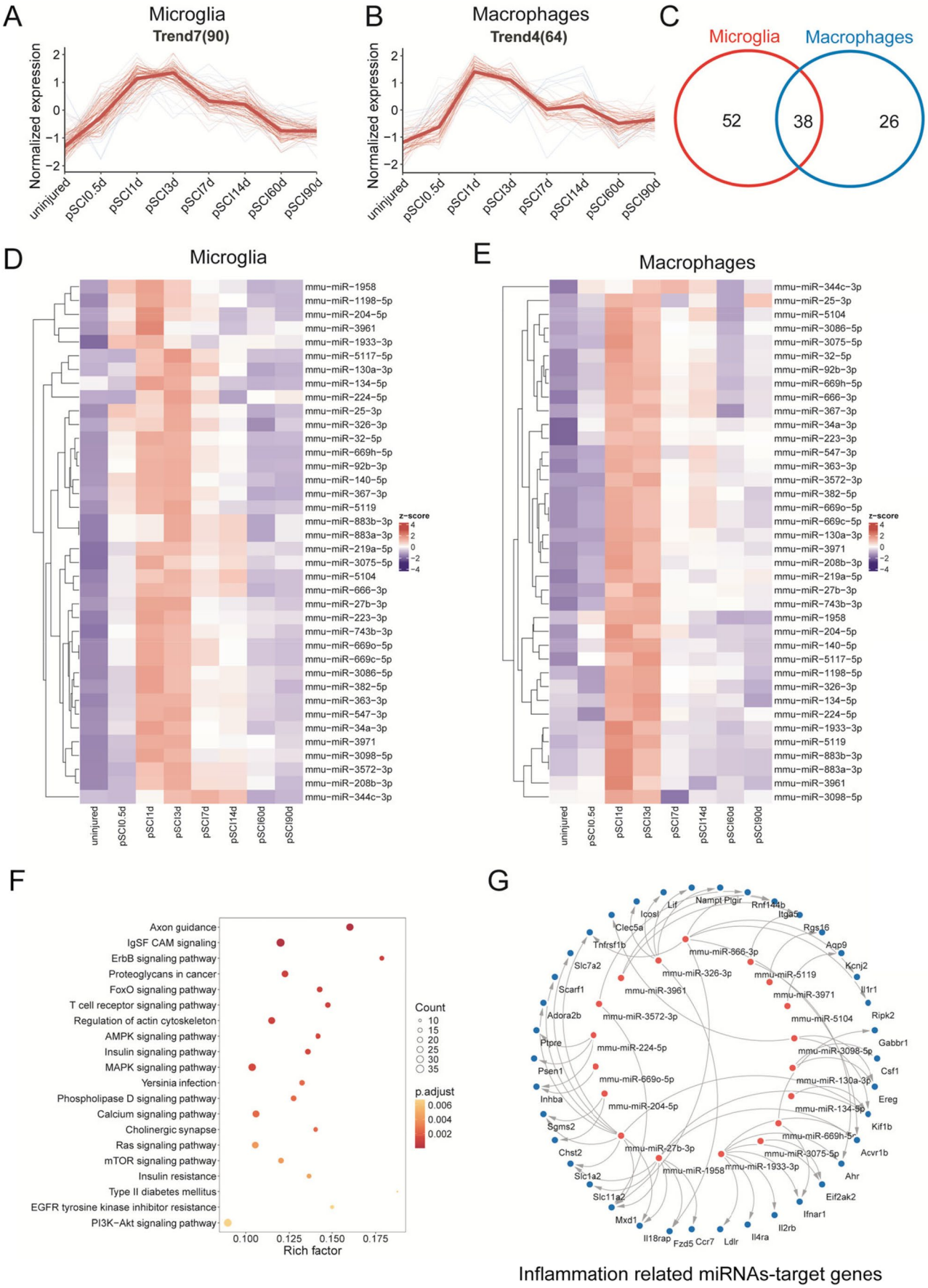
A
Microglia
Trend7(90)
Normalized expression
uninjured
pSCI0.5d
pSCI1d
pSCI3d
pSCI7d
pSCI14d
pSCI60d
pSCI90d
B
Macrophages
Trend4(64)
C
Microglia
Macrophages
52
38
26
D
Microglia
mmu-miR-1958
mmu-miR-1198-5p
mmu-miR-204-5p
mmu-miR-3961
mmu-miR-1933-3p
mmu-miR-5117-5p
mmu-miR-130a-3p
mmu-miR-134-5p
mmu-miR-224-5p
mmu-miR-25-3p
mmu-miR-326-3p
mmu-miR-32-5p
mmu-miR-669h-5p
mmu-miR-92b-3p
mmu-miR-140-5p
mmu-miR-367-3p
mmu-miR-5119
mmu-miR-883b-3p
mmu-miR-883a-3p
mmu-miR-219a-5p
mmu-miR-3075-5p
mmu-miR-5104
mmu-miR-666-3p
mmu-miR-27b-3p
mmu-miR-223-3p
mmu-miR-743b-3p
mmu-miR-669o-5p
mmu-miR-669c-5p
mmu-miR-3086-5p
mmu-miR-382-5p
mmu-miR-363-3p
mmu-miR-547-3p
mmu-miR-34a-3p
mmu-miR-3971
mmu-miR-3098-5p
mmu-miR-3572-3p
mmu-miR-208b-3p
mmu-miR-344c-3p
z-score
E
Macrophages
mmu-miR-344c-3p
mmu-miR-25-3p
mmu-miR-5104
mmu-miR-3086-5p
mmu-miR-3075-5p
mmu-miR-32-5p
mmu-miR-92b-3p
mmu-miR-669h-5p
mmu-miR-666-3p
mmu-miR-367-3p
mmu-miR-34a-3p
mmu-miR-223-3p
mmu-miR-547-3p
mmu-miR-363-3p
mmu-miR-3572-3p
mmu-miR-382-5p
mmu-miR-669o-5p
mmu-miR-669c-5p
mmu-miR-130a-3p
mmu-miR-3971
mmu-miR-208b-3p
mmu-miR-219a-5p
mmu-miR-27b-3p
mmu-miR-743b-3p
mmu-miR-1958
mmu-miR-204-5p
mmu-miR-140-5p
mmu-miR-5117-5p
mmu-miR-1198-5p
mmu-miR-326-3p
mmu-miR-134-5p
mmu-miR-224-5p
mmu-miR-1933-3p
mmu-miR-5119
mmu-miR-883b-3p
mmu-miR-883a-3p
mmu-miR-3961
mmu-miR-3098-5p
z-score
F
Axon guidance
IgSF CAM signaling
ErbB signaling pathway
Proteoglycans in cancer
FoxO signaling pathway
T cell receptor signaling pathway
Regulation of actin cytoskeleton
AMPK signaling pathway
Insulin signaling pathway
MAPK signaling pathway
Yersinia infection
Phospholipase D signaling pathway
Calcium signaling pathway
Cholinergic synapse
Ras signaling pathway
mTOR signaling pathway
Insulin resistance
Type II diabetes mellitus
EGFR tyrosine kinase inhibitor resistance
PI3K−Akt signaling pathway
0.100
0.125
0.150
0.175
Rich factor
Count
10
15
20
25
30
35
p.adjust
0.006
0.004
0.002
G
Lif
Nampt
Plgir
Rnf144b
Itga5
Icosl
Clec5a
Rgs16
Tnfrsf1b
Aqp9
mmu-miR-866-3p
Slc7a2
mmu-miR-326-3p
mmu-miR-5119
Kcnj2
Scarf1
mmu-miR-3961
mmu-miR-3971
Il1r1
Adora2b
mmu-miR-3572-3p
mmu-miR-5104
Ripk2
Ptpre
mmu-miR-224-5p
mmu-miR-3098-5p
Gabbr1
Psen1
mmu-miR-669o-5p
mmu-miR-130a-3p
Csf1
Inhba
mmu-miR-204-5p
mmu-miR-134-5p
Ereg
Sgms2
mmu-miR-669h-5p
Kif1b
Chst2
mmu-miR-27b-3p
mmu-miR-3075-5p
Acvr1b
Slc1a2
mmu-miR-1958
mmu-miR-1933-3p
Ahr
Slc11a2
Eif2ak2
Mxd1
Ifnar1
Il18rap
Fzd5
Ccr7
Ldlr
Il4ra
Il2rb
Inflammation related miRNAs-target genes

Fig. 5 miRNA–target–inflammatory pathway regulatory network analysis in microglia and macrophages. (**A**–**C**) Venn diagram illustrating 38 common differentially active miRNAs shared between microglia (Trend7) and macrophages (Trend4). (**D**) Heatmap showing the expression of the 38 common miRNAs in microglia. (**E**) Heatmap showing the expression of the 38 common miRNAs in macrophages. (**F**) Bubble plot of KEGG pathway enrichment analysis for target genes of common miRNAs. Color indicates adjusted p-value; bubble size indicates gene count. (**G**) miRNA–target–inflammatory pathway (INFLAMMATORY_RESPONSE) interaction network. Red nodes represent miRNAs; blue nodes represent target genes

during SCI progression. This atlas not only successfully identified miRNAs known to play key roles in neuroinflammation, such as miR-124-3p and miR-21a-5p (Liu et al. 2021, Yu et al. 2022), but also revealed several miRNAs with shared activity across multiple cell types, suggesting their potential involvement in cross-cellular cooperative pathological processes.

We acknowledge an important consideration regarding the computational nature of our miRNA activity inferences. The activity scores presented are derived from mRNA expression data and motif enrichment rather than direct measurements of miRNA abundance. To address this limitation, we performed an orthogonal validation using an independent bulk miRNA sequencing dataset (GSE90452). The significant concordance between computationally inferred activity changes and experimentally measured miRNA expression—with mmu-miR-488-3p, mmu-miR-300-3p, and mmu-miR-16b-3p showing both increased inferred activity and elevated expression, and mmu-miR-200a-3p, mmu-miR-132-3p, and mmu-miR-129-5p showing concordant decreases. Notably, these findings are consistent with previous studies reporting the involvement of these miRNAs in SCI pathology. miR-488-3p has been shown to regulate astrocyte inflammatory status and promote functional recovery after SCI, and its upregulation following injury has been documented in multiple independent studies (Pan et al. 2021). Similarly, miR-132-3p has been demonstrated to modulate macrophage M1 polarization and alleviate spinal cord ischemia-reperfusion injury(Fang et al. 2021), while miR-129-5p is well-established as a neuroprotective miRNA that suppresses apoptosis and inflammatory responses through targeting HMGB1/TLR4/NF-κB pathway (Wang et al. 2022, Li et al. 2020). This multi-dimensional validation strengthens confidence in the inferred regulatory networks while acknowledging that further experimental confirmation using single-cell small RNA sequencing or spatial transcriptomics would be valuable.

Microglia and macrophages play central roles in the inflammatory response after SCI, and the balance of their phenotypic polarization (M1 pro-inflammatory vs. M2 pro-repair) directly influences injury outcomes and repair (Ge et al. 2025, Brennan et al. 2022). Our study found that miRNAs with significantly altered activity in these two cell types were highly enriched in pathways such as TNF-α/NF-κB signaling, Toll-like receptor signaling, and cytokine signaling, consistent with previously reported roles of miRNAs in neuroinflammation (Liu et al. 2024, Li et al. 2024). Notably, the strong concordance between miRNA target enrichment and differential gene expression analysis—both converging on identical inflammatory pathways—provides orthogonal validation that the dynamic changes in miRNA activity are functionally relevant and actively shape the immune cell transcriptome. For instance, miR-155-5p has been shown to promote macrophage polarization toward an M1 phenotype (Prevost et al. 2025), whereas miR-146a-5p exerts protective effects by negatively regulating inflammatory signaling through feedback mechanisms (Zhou et al. 2024). The upregulation of these two miRNAs in macrophages in our study further supports their crucial roles in regulating inflammation during SCI.

Moreover, for the first time, we identified 38 common differentially active miRNAs shared between microglia and macrophages and constructed an miRNA–target–inflammatory pathway interaction network. Network analysis revealed that multiple common miRNAs (e.g., miR-27b-3p, miR-130a-3p) cooperatively targeted key inflammatory genes such as Lif, Csf1, and Il18rap, suggesting potential functional synergy between these two cell types at the post-transcriptional level during inflammatory responses. Experimental validation confirmed that miR-130a-3p promotes microglial inflammation, as its inhibition significantly attenuated LPS-induced TNF-α and IL-6 secretion in BV-2 cells. This direct functional evidence supports the pro-inflammatory role predicted by our computational analysis and exemplifies the value of integrating in silico predictions with in vitro experimentation.

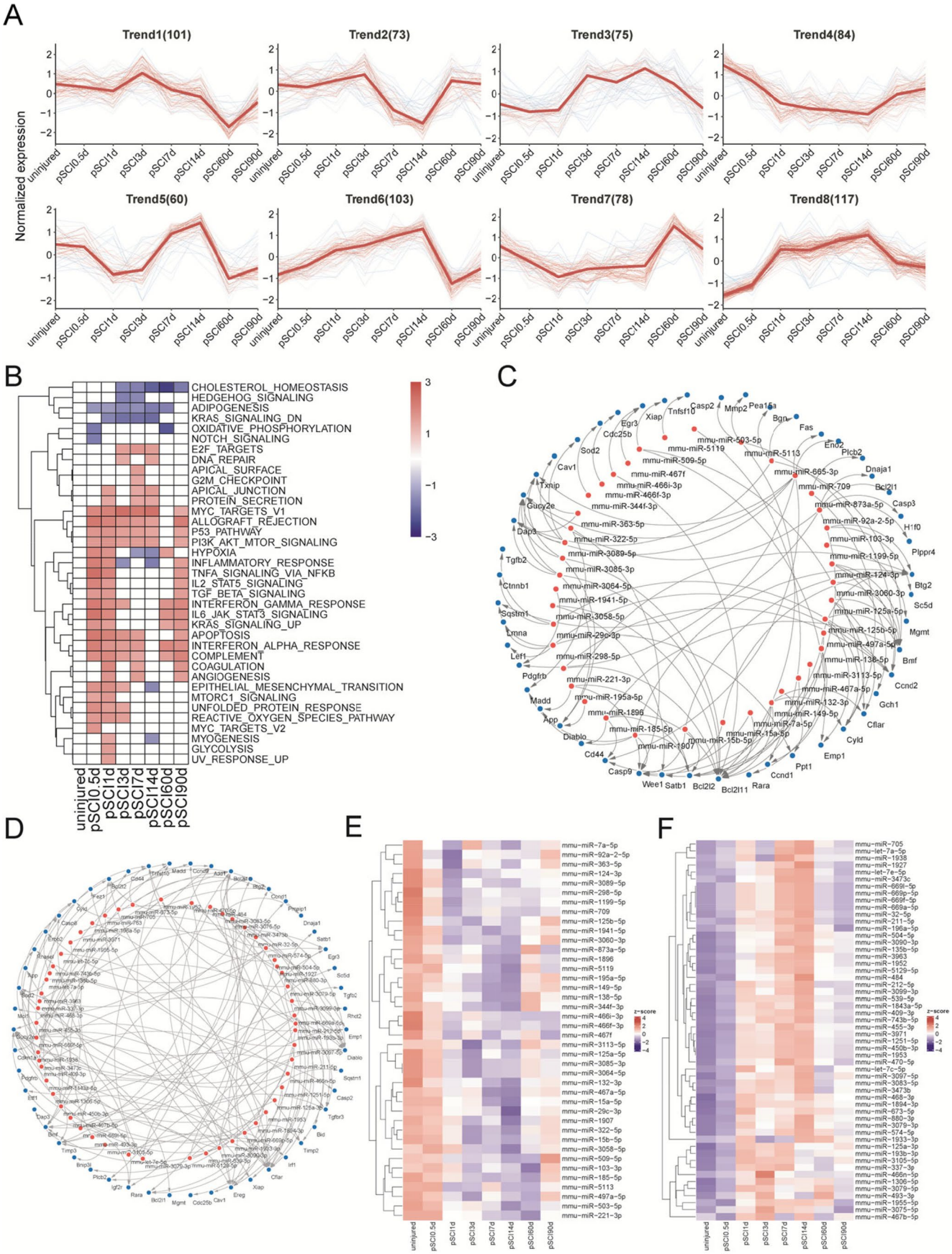
A
Trend1(101)
Trend2(73)
Trend3(75)
Trend4(84)
Trend5(60)
Trend6(103)
Trend7(78)
Trend8(117)
Normalized expression
uninjured
pSCI0.5d
pSCI1d
pSCI3d
pSCI7d
pSCI14d
pSCI60d
pSCI90d
B
CHOLESTEROL_HOMEOSTASIS
HEDGEHOG_SIGNALING
ADIPOGENESIS
KRAS_SIGNALING_DN
OXIDATIVE_PHOSPHORYLATION
NOTCH_SIGNALING
E2F_TARGETS
DNA_REPAIR
APICAL_SURFACE
G2M_CHECKPOINT
APICAL_JUNCTION
PROTEIN_SECRETION
MYC_TARGETS_V1
ALLOGRAFT_REJECTION
P53_PATHWAY
PI3K_AKT_MTOR_SIGNALING
HYPOXIA
INFLAMMATORY_RESPONSE
TNFA_SIGNALING_VIA_NFKB
IL2_STAT5_SIGNALING
TGF_BETA_SIGNALING
INTERFERON_GAMMA_RESPONSE
IL6_JAK_STAT3_SIGNALING
KRAS_SIGNALING_UP
APOPTOSIS
INTERFERON_ALPHA_RESPONSE
COMPLEMENT
COAGULATION
ANGIOGENESIS
EPITHELIAL_MESENCHYMAL_TRANSITION
MTORC1_SIGNALING
UNFOLDED_PROTEIN_RESPONSE
REACTIVE_OXYGEN_SPECIES_PATHWAY
MYC_TARGETS_V2
MYOGENESIS
GLYCOLYSIS
UV_RESPONSE_UP
C
D
E
F
z-score

Fig. 6 Mechanisms of miRNA-mediated regulation of apoptotic pathways in astrocytes. (**A**) Mfuzz trend analysis of miRNA activity changes in astrocytes, identifying 8 dynamic trends. Numbers on the right indicate the number of miRNAs in each trend. (**B**) Heatmap of GSEA functional enrichment analysis for target genes of differentially active miRNAs. Color represents NES. (**C**) miRNA–target–apoptosis pathway (APOPTOSIS) interaction network. (**D**) miRNA–target-P53 pathway interaction network. (**E**) Heatmap illustrating the temporal activity patterns of key apoptosis-regulating miRNAs in astrocytes across time points. Color represents z-score. (**F**) Heatmap illustrating the temporal activity patterns of key P53-regulating miRNAs in astrocytes across time points. Color represents z-score

Astrocytes are crucial for maintaining central nervous system homeostasis, and their apoptosis and dysfunction following SCI are important contributors to secondary injury (Patabendige et al. 2021, Hou et al. 2022). Our study found that certain miRNAs in astrocytes (e.g., miR-124-3p, miR-15b-5p) were significantly upregulated after injury, and their target genes were enriched in apoptotic pathways, participating in cell death by regulating key genes such as Casp3, Bcl2 family members, and Fas. This echoes previous findings that miR-124 promotes microglial apoptosis by targeting STAT3 (Li et al. 2025, Periyasamy et al. 2018), suggesting that miR-124 may participate in apoptosis regulation through different targets in different cell types. Experimental validation in C8-D1A astrocytes confirmed that miR-7a-5p mimic transfection exacerbated H_2O_2-induced apoptosis and increased cleaved caspase-3 levels, providing direct evidence for its pro-apoptotic function. This convergence of computational prediction and experimental verification strengthens the credibility of the proposed regulatory networks.

Additionally, we observed that apoptosis-related miRNAs were simultaneously enriched in both TNF signaling and p53 pathways, indicating close cross-regulation between inflammation and apoptosis in SCI. Previous studies have shown that TNF-α can induce astrocyte apoptosis by activating caspase cascades, and the p53 pathway plays a key role in DNA damage stress responses (Wang et al. 2019). The simultaneous regulation of these two pathways by miRNAs in our study further highlights their hub role in coordinating cellular stress responses.

This study has several limitations. First, although we validated inferred activity patterns using bulk miRNA sequencing data, single-cell resolution validation using techniques such as single-cell small RNA sequencing or spatial transcriptomics would provide deeper insights into cell type-specific miRNA expression. Second, the functional roles of additional key miRNAs identified in our networks (e.g., miR-27b-3p, miR-124-3p) require further experimental investigation. Third, while our in vitro experiments support the pro-inflammatory and pro-apoptotic functions of selected miRNAs, in vivo validation using animal models of SCI would be essential for translational applications. Future studies could employ CRISPR screening, miRNA agomir/antagomir approaches, and multi-omics integration to systematically elucidate miRNA regulatory networks in SCI.

Nonetheless, this study presents the first single-cell resolution map of computationally inferred and experimentally supported miRNA activity dynamics after SCI, providing in-depth insights into their regulatory roles in key pathological processes such as inflammation and apoptosis. The concordance across computational inference, independent dataset validation, and targeted experimentation enhances confidence in our findings and establishes a foundation for developing miRNA-based neuroprotective strategies.

Conclusion

In summary, this study provides a systematic, single-cell-resolution computational inference of miRNA activity dynamics and candidate functional networks in SCI, offering important theoretical foundations and data support for understanding its pathological mechanisms and developing targeted therapeutic strategies. Future research should integrate functional experiments and multi-omics approaches to advance the translational application of miRNAs in spinal cord injury repair.

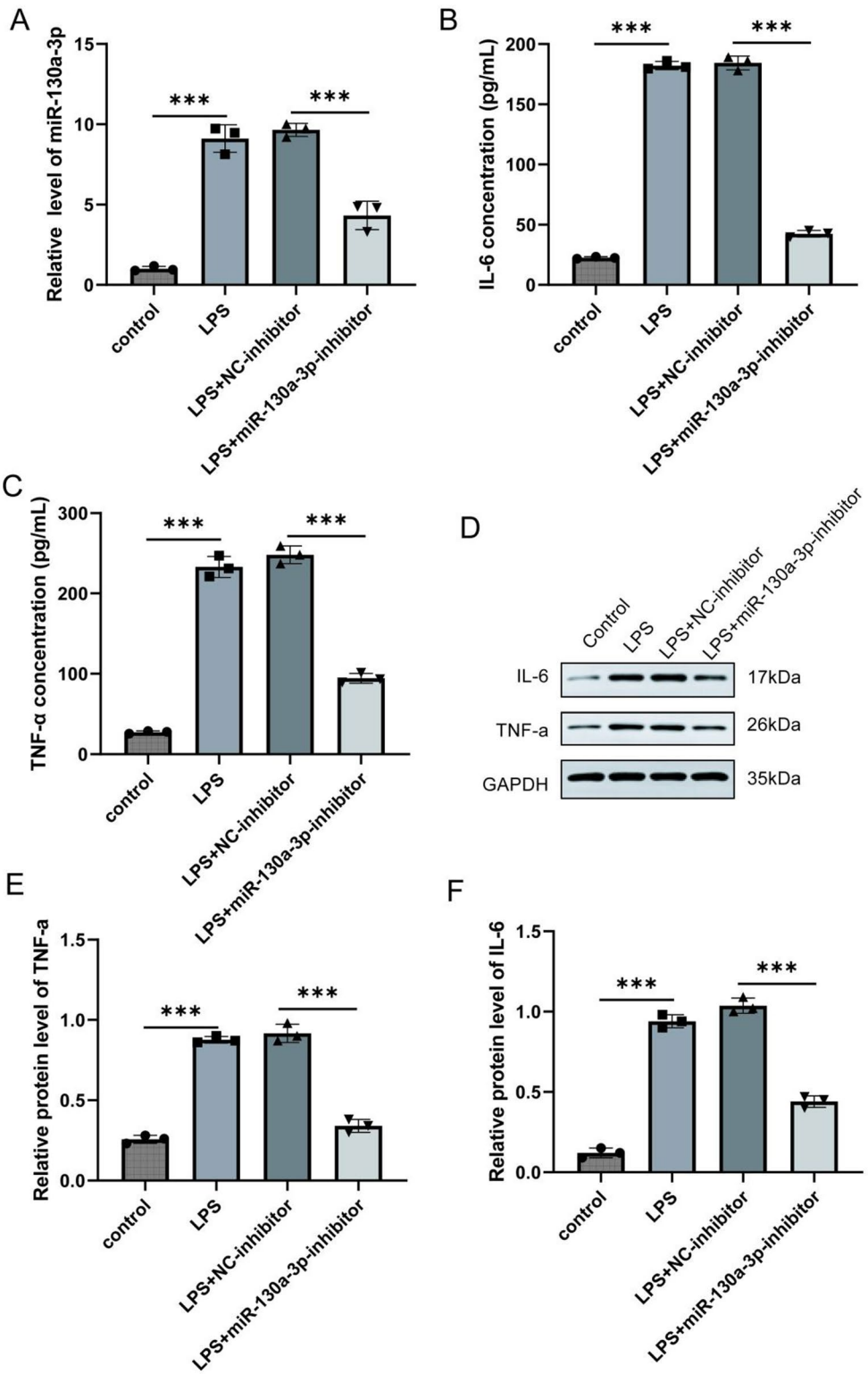

Fig. 7 Experimental validation of miR-130a-3p pro-inflammatory function in BV-2 microglial cells. (**A**) qRT-PCR analysis of miR-130a-3p expression under indicated conditions. LPS stimulation (100 ng/mL, 24 h) significantly upregulated miR-130a-3p, which was reversed by miR-130a-3p inhibitor transfection. (**B**, **C**) ELISA quantification of TNF-α (**B**) and IL-6 (**C**) secretion in culture supernatants. miR-130a-3p inhibition significantly attenuated LPS-induced cytokine release. (**D**) Representative western blot images showing TNF-α, IL-6, and GAPDH protein levels. (**E**, **F**) Quantification of relative protein levels of TNF-α (**E**) and IL-6 (**F**). Results confirm reduced inflammatory cytokine production upon miR-130a-3p inhibition. All bar graphs represent mean ± SD ($n = 3$ independent experiments), with individual data points overlaid as scatter symbols. *$p < 0.05$, **$p < 0.01$, ***$p < 0.001$

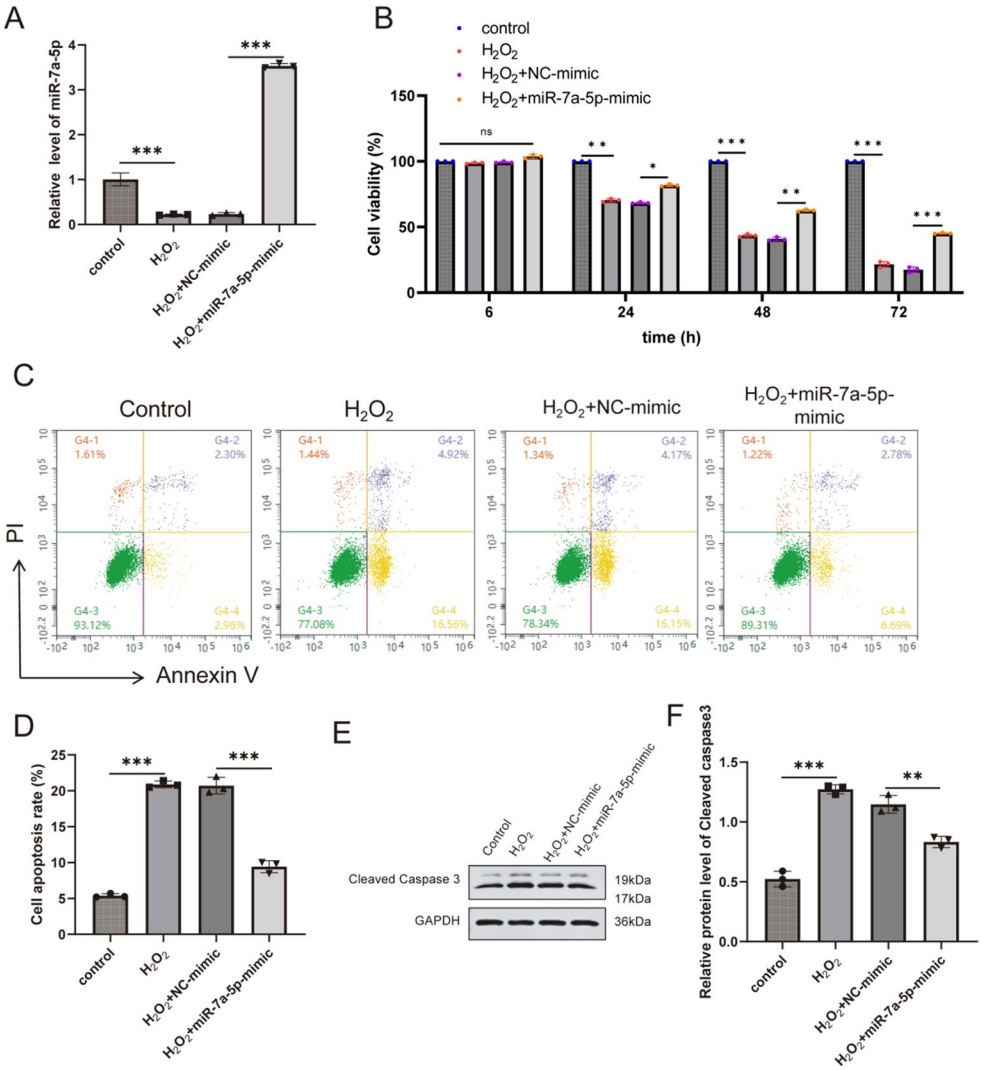

Fig. 8 Experimental validation of miR-7a-5p pro-apoptotic function in C8-D1A astrocytes. (**A**) qRT-PCR analysis of miR-7a-5p expression under indicated conditions. H_2O_2 treatment (200 µM, 12 h) significantly upregulated miR-7a-5p, which was further enhanced by miR-7a-5p mimic transfection. (**B**) CCK-8 cell viability assay showing that miR-7a-5p mimic transfection significantly rescued viability of H_2O_2-treated C8-D1A cells. (**C**) Representative flow cytometry plots of Annexin V/PI staining. (**D**) Quantification of apoptosis rate showing that miR-7a-5p mimic significantly attenuated H_2O_2-induced apoptosis. (**E**) Representative western blot images showing cleaved caspase-3 and GAPDH protein levels. (**F**) Quantification of relative cleaved caspase-3 protein levels. miR-7a-5p mimic significantly reduced cleaved caspase-3 in H_2O_2-treated cells. All bar graphs represent mean ± SD ($n = 3$ independent experiments), with individual data points overlaid as scatter symbols. *$p < 0.05$, **$p < 0.01$, ***$p < 0.001$

Supplementary Information The online version contains supplementary material available at https://doi.org/10.1007/s12031-026-02528-7.

Author Contributions Changli Xu and Jianli Bu contributed to the study conception and design. Changli Xu, Bingxuan Wang and Zhengqiang Li carried out the experiments and data collection. Changli Xu and Suchi Qiao analyzed and interpreted the data. Changli Xu wrote the manuscript text. Jianli Bu substantively revised the manuscript. All authors reviewed the manuscript.

Funding This work was supported by the National Natural Science Foundation of China (No.81671199) and the "Yanzhen" Talent Plan and the Technology Innovation Incubation Program Project of the Bethune International Peace Hospital (2024FYMSXM08).

Data Availability No datasets were generated or analysed during the current study.

Declarations

Competing Interests The authors declare no competing interests.

References

Anjum A et al (2020) Spinal cord injury: pathophysiology, multimolecular interactions, and underlying recovery mechanisms. Int J Mol Sci 21(20):7533

Brennan FH et al (2022) Microglia coordinate cellular interactions during spinal cord repair in mice. Nat Commun 13(1):4096

Cao Y et al (2022) Single-cell RNA sequencing for traumatic spinal cord injury. FASEB J 36(12):e22656

Cavalcanti RR et al (2025) Neuroinflammation: targeting microglia for neuroprotection and repair after spinal cord injury. Front Immunol 16:1670650

Clyde D (2022) Target-directed microRNA degradation in Drosophila. Nat Rev Genet 23(12):713

Dogan B et al (2022) Integrated bioinformatics analysis of validated and circulating miRNAs in ovarian cancer. Genomics Inf 20(2):e20

Fang H et al (2021) MiR-132-3p modulates MEKK3-dependent NF-kappaB and p38/JNK signaling pathways to alleviate spinal cord ischemia-reperfusion injury by hindering M1 polarization of macrophages. Front Cell Dev Biol 9:570451

Gao P et al (2023) Pericyte-derived exosomal miR-210 improves mitochondrial function and inhibits lipid peroxidation in vascular endothelial cells after traumatic spinal cord injury by activating JAK1/STAT3 signaling pathway. J Nanobiotechnol 21(1):452

Ge X et al (2025) Metabolic reprogramming through histone lactylation in microglia and macrophages recruits CD8(+) T lymphocytes and aggravates spinal cord injury. Neuron 113(14):2280–2296e8

Hou J et al (2022) Heterogeneity analysis of astrocytes following spinal cord injury at single-cell resolution. FASEB J 36(8):e22442

Kumar L (2007) Mfuzz: a software package for soft clustering of microarray data. Bioinformation 2(1):5–7

Lai A et al (2024) Annulus fibrosus injury induces acute neuroinflammation and chronic glial response in dorsal root ganglion and spinal cord-an in vivo rat discogenic pain model. Int J Mol Sci 25(3):1762

Li P et al (2024) Transplantation of miR-145a-5p modified M2 type microglia promotes the tissue repair of spinal cord injury in mice. J Transl Med 22(1):724

Liu F, Qiu F, Chen H (2021) miR-124-3p ameliorates isoflurane-induced learning and memory impairment via targeting STAT3 and inhibiting neuroinflammation. Neuroimmunomodulation 28(4):248–254

Liu J et al (2024) IPSC-NSCs-derived exosomal let-7b-5p improves motor function after spinal cord Injury by modulating microglial/macrophage pyroptosis. J Nanobiotechnol 22(1):403

Li Z et al (2020) Physical exercise ameliorates the cognitive function and attenuates the neuroinflammation of Alzheimer's disease via miR-129-5p. Dement Geriatr Cogn Disord 49(2):163–169

Li Z et al (2025) A reactive oxygen species-responsive hydrogel loaded with Apelin-13 promotes the repair of spinal cord injury by regulating macrophage M1/M2 polarization and neuroinflammation. J Nanobiotechnol 23(1):12

Lu TX, Rothenberg ME (2018) MicroRNA J Allergy Clin Immunol 141(4):1202–1207

Ma P et al (2023) Bacterial droplet-based single-cell RNA-seq reveals antibiotic-associated heterogeneous cellular states. Cell 186(4):877–891e14

Nielsen MM, Pedersen JS (2021) miRNA activity inferred from single cell mRNA expression. Sci Rep 11(1):9170

Olgun G, Gopalan V, Hannenhalli S (2022) miRSCAPE - inferring miRNA expression from scRNA-seq data. iScience 25(9):104962

Pan W et al (2021) lncRNA myocardial infarction-associated transcript (MIAT) knockdown alleviates LPS-induced chondrocytes inflammatory injury via regulating miR-488-3p/sex determining region Y-related HMG-box 11 (SOX11) axis. Open Life Sci 16(1):511–522

Patabendige A et al (2021) Astrocyte activation in neurovascular damage and repair following ischaemic stroke. Int J Mol Sci 22(8):4280

Periyasamy P et al (2018) Epigenetic promoter DNA methylation of miR-124 promotes HIV-1 Tat-mediated microglial activation via MECP2-STAT3 axis. J Neurosci 38(23):5367–5383

Prevost M et al (2025) The Resistin/TLR4/miR-155-5p axis: a novel signaling pathway in the onset of hypothalamic neuroinflammation. J Neuroinflammation 22(1):198

Qin C et al (2023) Advances in conductive hydrogel for spinal cord injury repair and regeneration. Int J Nanomed 18:7305–7333

Saraswathy VM, Zhou L, Mokalled MH (2024) Single-cell analysis of innate spinal cord regeneration identifies intersecting modes of neuronal repair. Nat Commun 15(1):6808

Silvestro S, Mazzon E (2022) MiRNAs as promising translational strategies for neuronal repair and regeneration in spinal cord injury. Cells 11(14):2177

Sirkis DW et al (2023) Single-cell RNA-seq reveals alterations in peripheral CX3CR1 and nonclassical monocytes in familial tauopathy. Genome Med 15(1):53

Sunshine MD et al (2023) Oxygen therapy attenuates neuroinflammation after spinal cord injury. J Neuroinflammation 20(1):303

Tansley S et al (2022) Single-cell RNA sequencing reveals time- and sex-specific responses of mouse spinal cord microglia to peripheral nerve injury and links ApoE to chronic pain. Nat Commun 13(1):843

Wang B et al (2024) Improving gene set enrichment analysis (GSEA) by using regulation directionality. Microbiol Spectr 12(3):e0345623

Wang C et al (2024) A single-cell and spatial RNA-seq database for Alzheimer's disease (ssREAD). Nat Commun 15(1):4710

Wang JL, Luo X, Liu L (2019) Targeting CARD6 attenuates spinal cord injury (SCI) in mice through inhibiting apoptosis, inflammation and oxidative stress associated ROS production. Aging 11(24):12213–12235

Wang T et al (2025) Spinal cord injury and ageing: the role of chronic neuroinflammation. Aging Dis

Wang Y et al (2022) Neuroprotective effect of HOTAIR silencing on isoflurane-induced cognitive dysfunction via sponging microRNA-129-5p and inhibiting neuroinflammation. Neuroimmunomodulation 29(4):369–379

Xiong W et al (2022) Treg cell-derived exosomes miR-709 attenuates microglia pyroptosis and promotes motor function recovery after spinal cord injury. J Nanobiotechnol 20(1):529

Yao C et al (2022) Single-cell sequencing reveals microglia induced angiogenesis by specific subsets of endothelial cells following spinal cord injury. FASEB J 36(7):e22393

Yu Z et al (2022) TNF-alpha stimulation enhances the neuroprotective effects of gingival MSCs derived exosomes in retinal ischemia-reperfusion injury via the MEG3/miR-21a-5p axis. Biomaterials 284:121484

Zhang Q et al (2023) Combination of single-cell and bulk RNA seq reveals the immune infiltration landscape and targeted therapeutic drugs in spinal cord injury. Front Immunol 14:1068359

Zhang X et al (2023) Single-cell analysis of the miRNA activities in tuberculous meningitis (TBM) model mice injected with the BCG vaccine. Int Immunopharmacol 124Pt A:p110871

Zhou H et al (2024) MicroRNA-146a-5p protects retinal ganglion cells through reducing neuroinflammation in experimental glaucoma. Glia 72(11):2115–2141